



DIPLOMARBEIT

DFT STUDIES OF GRAPHENE
INTERCALATION SYSTEMS:
GRAPHENE/Ni/IR AND
GRAPHENE/Ag/Re

ausgeführt am

Institut für Angewandte Physik
der Technischen Universität Wien

Institute for Applied Physics
Vienna University of Technology

unter der Anleitung von

Ao.Univ.Prof. Dipl.-Ing. Dr.techn. Josef Redinger

und

Dipl.-Ing. Dr.techn. Florian Mittendorfer

durch

Jörg Doppler, BSc

Schalkgasse 2/21

A-1180 Wien

jd@cms.tuwien.ac.at

Ort, Datum

Unterschrift

Jörg Doppler,
Schalkgasse 2/21, 1180 Wien

Hiermit erkläre ich, dass ich diese Arbeit selbständig verfasst habe, dass ich die verwendeten Quellen und Hilfsmittel vollständig angegeben habe und dass ich die Stellen der Arbeit einschließlich Tabellen, Karten und Abbildungen, die anderen Werken oder dem Internet im Wortlaut oder dem Sinn nach entnommen sind, auf jeden Fall unter Angabe der Quelle als Entlehnung kenntlich gemacht habe.

Ort, Datum

Unterschrift

Abstract

Intercalation of Ni under graphene/Ir(111). To gain insight into the intercalation of metal layers in-between graphene (Gr) and its supporting substrate, we investigate the diffusion processes of a single nickel atom through a graphene sheet which is adsorbed on Ir(111). Utilizing the ab-initio DFT code VASP, the intercalation is assessed numerically for different instances of the system, starting with diffusion through an unsupported graphene sheet. Both an ideal graphene layer as well as a layer featuring a vacant carbon site are taken into account. The process is modelled by tuning the vertical distance of the Ni atom with respect to the surface in each numerical run, followed by a full relaxation of the nearest carbon atoms. The energy vs. reaction coordinate data is then used to determine the transition state of the particular reaction in more detail by means of the dimer method, for which VASP offers a systematic approach for finding saddle points on high-dimensional potential energy surfaces and thus the reaction mechanism. Having obtained the transition state, the corresponding cell geometry is placed on an Ir(111) support. We find that, if assessing the data for unsupported graphene layers, the diffusion through a pristine sheet is facing a barrier of about 12 eV, which is very large and extremely unlikely to be overcome at typical annealing temperatures. However, at a vacancy, this barrier is lowered significantly to about 2 eV. A further decrease of approximately 0.5 eV is obtained if the vacant graphene is placed on top of the Ir(111) substrate.

Graphene/Ag(111)/Re(0001). Data from angle-resolved photoemission spectra (ARPES) on graphene/Re and graphene/Ag/Re, which features an additional intercalated Ag monolayer, demonstrates that the decoupling of graphene (Gr) from the Re substrate is not as pronounced as expected as soon as Ag is introduced. The Ag layer grows epitaxially, and there is evidence of a hybridization of the Ag bands with graphene's π -state. We study the electronic structure of Gr/Ag(111)/Re(0001) by means of numerical ab-initio DFT calculations employing the VASP code. The properties of Gr/Ag/Re are determined in a simplified approach by studying a primitive (1x1) cell for both the lattice constant of Re and Gr, i.e. either stretching Gr or compressing the underlying Ag/Re substrate, respectively. Different interface mod-

els and graphene-substrate distances were tested to determine the energetically most favorable placement of the carbon atoms relative to the substrate surface, yielding the top-fcc arrangement, i.e. one C on top of Ag and the other on the fcc hollow site, as the structure featuring the lowest energy. Due to interaction with the Ag/Re substrate, the electronic structure of graphene is modified, showing good agreement with the above mentioned ARPES experiments. We observe a downward shift of the Dirac point with respect to the Fermi energy and also a hybridization of the graphene π -band with the Ag d-bands. The magnitude of both phenomena is shown to depend on the graphene-substrate distance.

Kurzfassung

Interkalation von Ni unter Graphen/Ir(111). Um einen Einblick in die Interkalation von Metallschichten zwischen Graphen (Gr) und einem tragenden Substrat zu erhalten untersuchen wir Diffusionsprozesse eines einzelnen Nickel Atoms durch eine auf Ir(111) adsorbierte Graphen Schicht. Die Interkalation wird numerisch mit Hilfe des ab-initio DFT Codes VASP für verschiedene Realisierungen des Systems untersucht, angefangen mit der Diffusion eines Ni Atoms durch eine freie Graphen Lage. Wir betrachten sowohl ideales Graphen als auch eine Graphen Schicht mit Fehlstellen. Der Prozess selbst wird untersucht indem zunächst der vertikale Abstand des Ni Atoms von der Graphen Oberfläche sukzessive verringert wird. In jedem Schritt wird eine volle Relaxation der benachbarten C Atome zugelassen. Die auf diesem Wege erhaltenen Daten von Energie vs. Reaktionskoordinate ermöglichen in weiterer Folge die Bestimmung des Übergangszustandes mittels der Dimer-Methode, für welche VASP einen systematischen Algorithmus bereitstellt um Sattelpunkte auf der hochdimensionalen Energieoberfläche zu finden. Die Geometrie des Übergangszustandes wird dann auch anschließend auf die Ir(111) Oberfläche transferiert. Unsere Untersuchungen zeigen, dass für die Diffusion durch eine ideale, freie Graphen Schicht eine Energiebarriere von 12 eV überwunden werden muss, ein Wert der sehr hoch ist und daher einen sehr unwahrscheinlichen Mechanismus darstellt. Ist jedoch eine Fehlstelle im Graphen vorhanden, wird die Energiebarriere auf 2 eV reduziert. Eine weitere Reduktion um 0.5 eV wird erreicht sobald diese Graphen Schicht auf das Ir(111) Substrat aufgebracht wird.

Graphen/Ag(111)/Re(0001). Photoelektronenspektroskopie (engl. angle-resolved photoemission spectroscopy - ARPES) an Graphen/Re sowie an Graphen/Ag/Re, das eine zusätzliche interkalierte Monolage Ag aufweist, deutet darauf hin dass die Entkopplung von Graphen (Gr) vom Rhenium Substrat keineswegs so ausgeprägt ist wie erwartet. Weiters zeigt das Experiment, dass die Ag Lage epitaktisch aufwächst und eine Hybridisierung der Ag Bänder mit dem Graphen π -Zustand zeigt. Wir untersuchen die elektronische Struktur von Gr/Ag/Re mittels numerischen ab-initio DFT Rechnungen unter der Verwendung von VASP. Wir ermitteln die Eigenschaften dieses

Materials in einem vereinfachten Modell, indem wir eine primitive (1x1) Zelle verwenden. Die unterschiedlichen Gitterkonstanten von Graphen bzw. Rhenium machen es nötig, zwei gesonderte Fälle zu betrachten, nämlich entweder die Graphen Lage zu strecken bzw. das Ag/Re Substrat zu komprimieren. In diesen Systemen betrachten wir verschiedene Grenzflächen-Geometrien sowie Graphen-Substrat Abstände um die energetisch günstigste Lage der Kohlenstoff Atome zum Substrat zu bestimmen. Dabei finden wir, dass die top-fcc Struktur, d.h. ein C Atom über (top) einem Ag Atom und das andere in der fcc Lücke, diejenige mit der stabilsten energetischen Konfiguration ist. Aufgrund der Wechselwirkung mit dem Ag/Re Substrat wird die elektronische Struktur von Graphen modifiziert, was in guter Übereinstimmung mit dem oben genannten ARPES Experiment ist. Wir finden eine Absenkung des Dirac Punktes bezüglich der Fermi Energie und weiters eine Hybridisierung der Ag d-Bänder mit Graphens π -Band. Beide Phänomene hängen, wie gezeigt wird, stark vom Graphen-Substrat Abstand ab.

Contents

1	Introduction	8
2	Graphene	11
2.1	Tight-binding bandstructure	12
2.2	Dirac fermions	16
3	Method	18
3.1	Born-Oppenheimer approximation	19
3.2	Hartree and Hartree-Fock equations	20
3.3	Hohenberg-Kohn theorems and Kohn-Sham equations	21
3.4	Exchange-correlation functionals	24
3.5	Van-der-Waals interaction	25
3.5.1	Background	25
3.5.2	Implementation	28
4	Results	29
4.1	Intercalation process: Graphene/Ni/Ir(111)	30
4.1.1	Introduction	30
4.1.2	Numerics	31
4.1.2.1	Setup	31
4.1.2.2	Methods	32
4.1.2.3	Unsupported graphene	34
4.1.2.4	Supported graphene	38
4.2	Graphene/Ag(111)/Re(0001)	41
4.2.1	Experiment	41
4.2.2	Numerics	42
4.2.2.1	Setup	42
4.2.2.2	Lattice constants	42
4.2.2.3	Unit cell preparation	46
4.2.2.4	Bandstructure	48

5	Summary and Outlook	55
	Appendix	57
1	SGE job script	57
2	Visualize ionic relaxation	59
2.1	xmake.sh	60
2.2	visualizeRelaxation.sh	61
2.3	showUnstableModes.sh	62
3	Reaction coordinate	63
	Acknowledgements	66
	Bibliography	67
	List of Figures	70
	List of Tables	74

Chapter 1

Introduction

Ever since single-layered carbon planes were made experimentally accessible by K. Novoselov and A. Geim et al. in 2004, they have attracted much attention in the scientific community. Graphene (Gr), as this two dimensional material was termed, possesses a variety of favorable features, clearly distinguishing it from conventional, previously known materials. Most surprisingly in the first place was the very existence of planar graphene itself, in contrast to previous theoretical belief [1, 2].

Owing to its remarkable high purity, graphene exhibits, among others, ballistic transport, exceptionally high mobilities and the quantum Hall effect (QHE) even at room temperature. Furthermore, since graphene remains stable in the nanometer regime, it allows for single-electron-transistors and, combined with a reduced switching time, might embody the successor of silicon in the semiconductor industry's search for ever smaller devices [3]. Also, due to its linear dispersion relation at the Dirac point, charge carriers in graphene are described by massless quasiparticles which obey the relativistic Dirac equation rather than the Schroedinger equation. These quasiparticles are thus called Dirac fermions [4, 5, 6].

For completeness, we may add that scientific interest in carbon isn't solely limited to its two dimensional manifestation, but also focusses on its allotropes, i.e. fullerenes (0D), carbon nanotubes (1D) and graphite (3D).

With regard to possible future graphene based electronic devices, it is desirable to harness graphene's wide range of preferable characteristics. If, however, placed upon a substrate, these features might not be conserved or, at the worst, might get completely lost due to interaction with the support, rendering the specific graphene on metal interface unfeasible for particular applications.

Several substrates have been determined to show only a weak interaction with graphene, where, due to the weak bonding at distances greater than 3 Å, the physisorbed graphene layer almost exhibits its pristine electronic structure. Metals which belong to this class of materials are, for instance, Pt [7], Ir [8, 9] and Cu [10, 11].

In contrast, metals such as Ni [12, 13], Ru [14] or Rh [15, 16] display a much stronger interaction, resulting in a reduced distance between substrate and the chemisorbed graphene layer which is over 1 Å closer than in weakly interacting systems. As a result of the strong coupling, graphene’s unique electronic structure is destroyed.

It was found, however, that the addition of an intercalated noble metal layer can lead to a significant reduction of graphene’s coupling to the supporting substrate in these systems. Common perception thinks of this additional layer as a spacer layer which leads to a reduction of the overlap of the involved orbitals of graphene and its support, thus almost restoring the electronic features of a pristine graphene sheet.

In the present thesis, we investigate two different realizations of systems which belong to the topic of intercalation. Our first assessment will concern the question of how an intercalated layer is formed, while the effect of an intercalated layer on the graphene-substrate coupling is the subject of the subsequent investigation:

Intercalation of Ni under Gr/Ir(111). In the first part of this thesis, we are interested in the *formation* of the intercalated layer. This will be done by determining the energy barriers of the various reaction processes by means of ab-initio numerical density functional calculations employing the Vienna Ab-initio Simulation Package (VASP). More precisely, we model the diffusion of a single Nickel atom through graphene sheets which feature no or one vacant carbon site. Freestanding layers and graphene supported by iridium are considered.

Gr/Ag(111)/Re(0001). In the second part the Gr/Ag/Re system is examined, which features already an intercalated monolayer of silver. Opposed to the above mentioned common view, experimental data for this particular system suggest that the expected decoupling of graphene from the metal substrate after intercalation is actually significantly *less effective* than expected. We thus study the electronic structure of Gr/Ag/Re to reveal the nature of the observed deviation from currently known systems in which graphene is adsorbed on a noble metal/metal interface.

Both topics originated from collaborations with experimental groups participating in the EuroGRAPH/SpinGraph research project of the European Science Foundation (ESF), which are M. Fonin et al. of the University of Konstanz (Gr/Ni/Ir) and M. Papagno and coworkers in C. Carbone’s group at ELETTRA/Trieste (Gr/Ag/Re).

This thesis is structured as follows. Chapter 2 reviews the electronic properties of graphene, focussing on its bandstructure as obtained by the tight-binding model. In chapter 3 we introduce the basics of the methods which are used in the VASP code, namely Density Functional Theory (DFT). Additionally, the Hartree theory and its

successor, the Hartree-Fock (HF) theory are covered. Representing the crucial quantity in DFT calculations and thus also in this current thesis, different approximations to the DFT exchange-correlation potential are briefly addressed. The results of our investigations of the diffusion of Ni under Gr/Ir as well as for Gr/Ag/Re are presented in chapter 4. In the last chapter, we conclude by briefly summarizing our findings and by providing an outlook for potential further investigations. The appendix provides additional information on useful shell scripts which were written in the course of the present thesis to allow a more convenient operation of VASP.

Chapter 2

Graphene

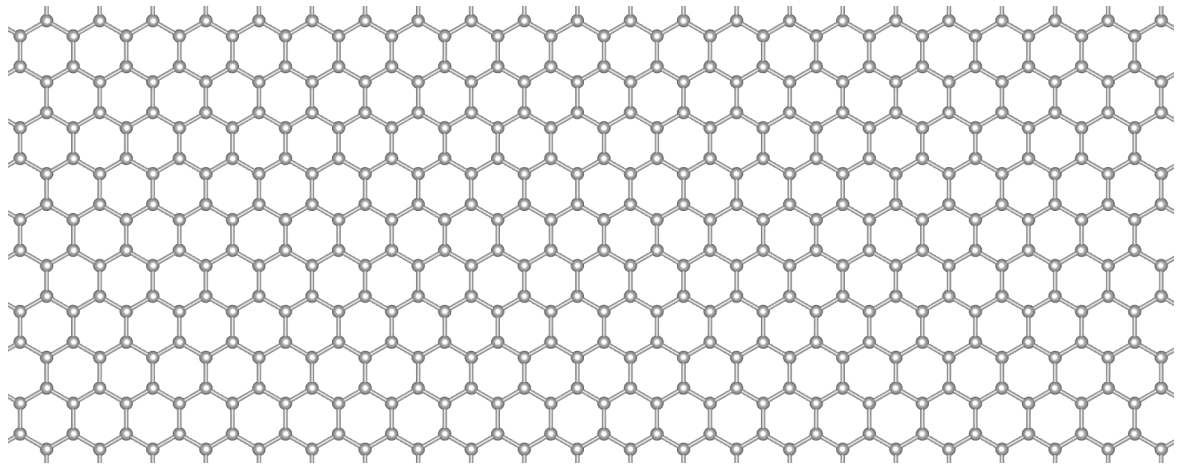


Figure 2.1: Honeycomb lattice of graphene.

Graphene, a perfectly two-dimensional carbon based material which crystallizes in a honeycomb lattice, has created an unparalleled amount of research since it was made experimentally accessible by K. Novoselov and A. Geim et al. in 2004. Surprisingly enough, the bandstructure of graphene has already been derived 65 years ago by P.R. Wallace while examining the electronic properties of bulk graphite [17].

In this section we want to give a concise treatment of selected remarkable properties of graphene. Since graphene's bandstructure represents an integral part of its fascinating features, and also due to its prominent role in this present thesis, we want to display the analytical tight-binding bandstructure calculation of graphene in the following section. Subsequently, the connection of graphene's electrons to ultrarelativistic particles is motivated.¹

¹This chapter's treatment largely follows Refs. [18, 19, 20].

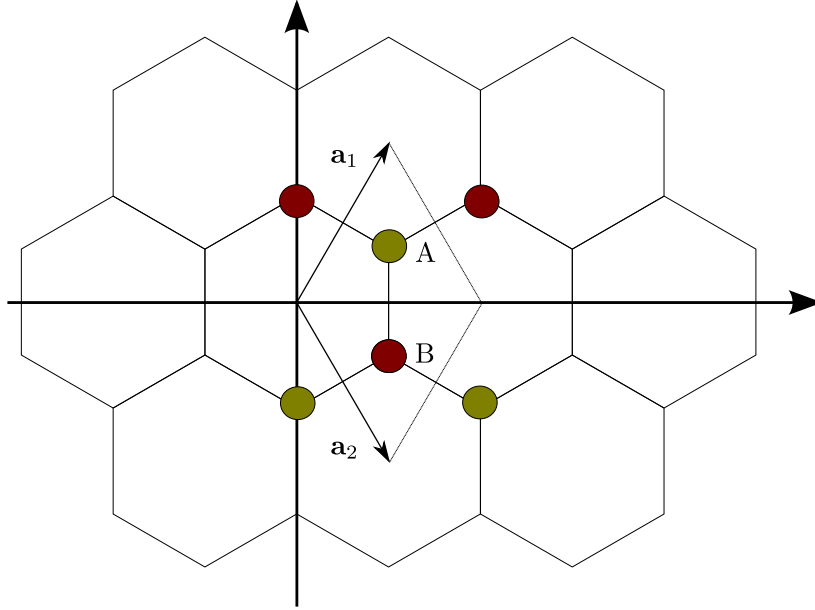


Figure 2.2: Unit cell of graphene. The two different sublattices are indicated by coloured circles.

2.1 Tight-binding bandstructure

Graphene is composed of carbon atoms which are arranged periodically to form a honeycomb lattice (see Fig. 2.1). The exceptional structural properties of graphene stem from the carbon atoms being bound by sp^2 -hybrid orbitals which establish σ - and π -bonds with neighboring in-plane sites. Carbon's electronic configuration reads $1s^2 2s^2 2p^2$, thus leaving four valence electrons for bonding. Three of these four valence electrons take part in the σ -bond, whereas one remaining electron occupies the p_z orbital. It is the latter which will form the π and π^* -bands of graphene and are thus our main object in this section.

The honeycomb structure is not a Bravais lattice but is rather characterized as a triangular lattice with a basis of two atoms per unit cell, A and B, as depicted in Fig. 2.2. At first we choose the primitive lattice vectors \mathbf{a}_1 and \mathbf{a}_2 as follows,

$$\mathbf{a}_1 = a \begin{pmatrix} \frac{1}{2} \\ \frac{\sqrt{3}}{2} \end{pmatrix} \quad \text{and} \quad \mathbf{a}_2 = a \begin{pmatrix} \frac{1}{2} \\ -\frac{\sqrt{3}}{2} \end{pmatrix}, \quad (2.1)$$

with a being the system's lattice constant. The coordinates of the atoms of the two sublattices A and B are then taken to be linear combinations of the primitive basis vectors \mathbf{a}_n with an additional position vector \mathbf{t}_i which points from a given lattice point

to an atom of sublattice A or B,

$$\begin{aligned}\mathbf{R}_{A,nm} &= n\mathbf{a}_1 + m\mathbf{a}_2 + \mathbf{t}_A = \mathbf{R}_{nm} + \mathbf{t}_A \\ \mathbf{R}_{B,nm} &= n\mathbf{a}_1 + m\mathbf{a}_2 + \mathbf{t}_B = \mathbf{R}_{nm} + \mathbf{t}_B.\end{aligned}\quad (2.2)$$

One then obtains the infinitely extended 2D graphene crystal by translating the unit cell to fill the whole two dimensional space. In the spirit of the LCAO approach, the wavefunction $|\Psi_{\mathbf{k}}(\mathbf{r})\rangle$ for the π -bonds is chosen as a linear combination of atomic orbitals $|\phi(\mathbf{r})\rangle$,

$$|\Psi_{\mathbf{k}}(\mathbf{r})\rangle = \frac{1}{\sqrt{N}} \sum_{\mathbf{R}_{nm}} e^{i\mathbf{k}\mathbf{R}_{nm}} [A |\phi(\mathbf{r} - \mathbf{R}_{A,nm})\rangle + B |\phi(\mathbf{r} - \mathbf{R}_{B,nm})\rangle]. \quad (2.3)$$

The coefficients A and B denote unknown amplitude parameters and N is the number of lattice sites in the crystal. The wavefunction $|\phi(\mathbf{r})\rangle$ corresponds to the p_z orbital of the sp^2 hybridized carbon atom. We might add that Eq. (2.3) can also be written in a form more reminiscent of Bloch's theorem, i.e.

$$|\Psi_{\mathbf{k}}(\mathbf{r})\rangle = e^{i\mathbf{k}\mathbf{r}} |u_{\mathbf{k}}(\mathbf{r})\rangle, \quad (2.4)$$

with

$$|u_{\mathbf{k}}(\mathbf{r})\rangle = \frac{1}{\sqrt{N}} \sum_{\mathbf{R}_{nm}} e^{-i(\mathbf{r}-\mathbf{k}\mathbf{R}_{nm})} [A |\phi(\mathbf{r} - \mathbf{R}_{A,nm})\rangle + B |\phi(\mathbf{r} - \mathbf{R}_{B,nm})\rangle], \quad (2.5)$$

which function has the required periodicity of the lattice. To have a more convenient form of Eq. (2.3), we rewrite it further,

$$|\Psi_{\mathbf{k}}(\mathbf{r})\rangle = A |\Psi_{\mathbf{k}}^A\rangle + B |\Psi_{\mathbf{k}}^B\rangle, \quad (2.6)$$

with the $|\Psi_{\mathbf{k}}^i\rangle$ given by.

$$|\Psi_{\mathbf{k}}^i\rangle = \frac{1}{\sqrt{N}} \sum_{\mathbf{R}_{nm}} e^{i\mathbf{k}\mathbf{R}_{nm}} |\phi_i(\mathbf{r} - \mathbf{R}_{i,nm})\rangle \quad (2.7)$$

The system's Hamiltonian is composed of the electron's kinetic energy, as well as the contribution of all carbon atoms from sublattices A and B, respectively,

$$H = \frac{\mathbf{p}^2}{2m_e} + \sum_{\mathbf{R}_{nm}} [V(\mathbf{r} - \mathbf{R}_{A,nm}) + V(\mathbf{r} - \mathbf{R}_{B,nm})]. \quad (2.8)$$

Applying H to $|\Psi_{\mathbf{k}}(\mathbf{r})\rangle$ and acting with $\langle\Psi_{\mathbf{k}}^i|$ from the left yields

$$\begin{aligned}\langle\Psi_{\mathbf{k}}^i|\hat{H}|\Psi_{\mathbf{k}}\rangle &= A \langle\Psi_{\mathbf{k}}^i|\hat{H}|\Psi_{\mathbf{k}}^A\rangle + B \langle\Psi_{\mathbf{k}}^i|\hat{H}|\Psi_{\mathbf{k}}^B\rangle \\ &= A H_{iA} + B H_{iB},\end{aligned}\tag{2.9}$$

$$\begin{aligned}&= E(\mathbf{k}) (A \langle\Psi_{\mathbf{k}}^i|\Psi_{\mathbf{k}}^A\rangle + B \langle\Psi_{\mathbf{k}}^i|\Psi_{\mathbf{k}}^B\rangle) \\ &= E(\mathbf{k}) (A S_{iA} + B S_{iB}),\end{aligned}\tag{2.10}$$

with the matrix elements $\langle\Psi_{\mathbf{k}}^i|\hat{H}|\Psi_{\mathbf{k}}^j\rangle = H_{ij}$ and $\langle\Psi_{\mathbf{k}}^i|\Psi_{\mathbf{k}}^j\rangle = S_{ij}$. Writing above equation in matrix form, we have

$$\begin{pmatrix} H_{AA} - E(\mathbf{k})S_{AA}(\mathbf{k}) & H_{AB} - E(\mathbf{k})S_{AB}(\mathbf{k}) \\ H_{AB}^* - E(\mathbf{k})S_{AB}^*(\mathbf{k}) & H_{BB} - E(\mathbf{k})S_{BB}(\mathbf{k}) \end{pmatrix} \begin{pmatrix} A \\ B \end{pmatrix} = \begin{pmatrix} 0 \\ 0 \end{pmatrix}.\tag{2.11}$$

To obtain the energy eigenvalues $E(\mathbf{k})$ we determine the roots of the secular equation,

$$E(\mathbf{k})^{\pm} = \frac{(2E_0 - E_1) \pm \sqrt{(2E_0 - E_1)^2 - 4E_2E_3}}{2E_3}\tag{2.12}$$

with the E_i abbreviated by

$$\begin{aligned}E_0 &= H_{AA}S_{AA}, & E_1 &= S_{AB}H_{AB}^* + H_{AB}S_{AB}^* \\ E_2 &= H_{AA}^2 - H_{AB}H_{AB}^*, & E_3 &= S_{AA}^2 - S_{AB}S_{AB}^*.\end{aligned}\tag{2.13}$$

Taking only the nearest-neighbor interaction into account, i.e. only the three adjacent lattice sites (see Fig. 2.2) contribute, we have

$$\begin{aligned}H_{AA} &= \frac{1}{N} \sum_{\mathbf{R}_{A,nm}} \sum_{\mathbf{R}_{A',nm}} e^{i\mathbf{k}(\mathbf{R}_{A',nm} - \mathbf{R}_{A,nm})} \langle\phi_A(\mathbf{r} - \mathbf{R}_{A,nm})|H|\phi_A(\mathbf{r} - \mathbf{R}_{A',nm})\rangle \\ &= \frac{1}{N} \sum_{\mathbf{R}_{A,nm}} \langle\phi_A(\mathbf{r} - \mathbf{R}_{A,nm})|H|\phi_A(\mathbf{r} - \mathbf{R}_{A,nm})\rangle = \epsilon_{2p},\end{aligned}\tag{2.14}$$

with N being the total number of primitive cells in the crystal. The vectors $\mathbf{R}_{A,nm}$ and $\mathbf{R}_{A',nm}$ determine the atomic positions of A and A' , respectively. Since the atomic wavefunctions are normalized, $S_{AA} = 1$, i.e.

$$\langle\phi_A(\mathbf{r} - \mathbf{R}_{A,nm})|\phi_A(\mathbf{r} - \mathbf{R}_{A,nm})\rangle = 1.\tag{2.15}$$

The same holds true for H_{BB} . H_{AB} is obtained by summing over the three nearest-neighbors,

$$\begin{aligned}
H_{AB} &= \frac{1}{N} \sum_{\mathbf{R}_{A,nm}} \sum_{\mathbf{R}_{B,nm}} e^{i\mathbf{k}(\mathbf{R}_{B,nm}-\mathbf{R}_{A,nm})} \langle \phi_A(\mathbf{r}-\mathbf{R}_{A,nm}) | H | \phi_B(\mathbf{r}-\mathbf{R}_{B,nm}) \rangle \\
&= \gamma_0 (e^{i\mathbf{k}\mathbf{R}_{11}} + e^{i\mathbf{k}\mathbf{R}_{12}} + e^{i\mathbf{k}\mathbf{R}_{13}}),
\end{aligned} \tag{2.16}$$

with

$$\gamma_0 = \langle \phi_A(\mathbf{r}-\mathbf{R}_{A,nm}) | H | \phi_B(\mathbf{r}-\mathbf{R}_{A,nm}-\mathbf{R}_{1i}) \rangle, \quad (i = 1, 2, 3). \tag{2.17}$$

Correspondingly,

$$S_{AB} = s_0 (e^{i\mathbf{k}\mathbf{R}_{11}} + e^{i\mathbf{k}\mathbf{R}_{12}} + e^{i\mathbf{k}\mathbf{R}_{13}}), \tag{2.18}$$

with

$$s_0 = \langle \phi_A(\mathbf{r}-\mathbf{R}_{A,nm}) | \phi_B(\mathbf{r}-\mathbf{R}_{A,nm}-\mathbf{R}_{1i}) \rangle, \quad (i = 1, 2, 3). \tag{2.19}$$

\mathbf{R}_{1i} is defined as the vector which points from the atomic site A to the nearest-neighbor atoms B . Inserting our findings into Eq. (2.12), we obtain

$$E(\mathbf{k})^\pm = \frac{\epsilon_{2p} \mp \gamma_0 \sqrt{f(\mathbf{k})}}{1 \mp s_0 \sqrt{f(\mathbf{k})}}, \tag{2.20}$$

where we introduced the function $f(\mathbf{k})$,

$$\begin{aligned}
f(\mathbf{k}) &= 3 + g(\mathbf{k}) \\
&= 3 + 2 \cos \mathbf{k} \cdot \mathbf{a}_1 + 2 \cos \mathbf{k} \cdot \mathbf{a}_2 + 2 \cos \mathbf{k} \cdot (\mathbf{a}_1 - \mathbf{a}_2)
\end{aligned} \tag{2.21}$$

In practice, the three parameters ϵ_{2p} , γ_0 and s_0 are determined by means of a fit to experimental or first-principles data. Fig. 2.1 shows the bandstructure for the choice of values $\epsilon_{2p} = 0$, $\gamma_0 = 2.7$ and $s_0 = 0.15$, as well as the density of states.

More precisely, part (a) of Fig. 2.1 displays graphene's π bands as obtained by Eq. (2.20) along lines of high symmetry in the first Brillouin zone, i.e. from K to Γ over M back to K (illustrated in Fig. 2.1 (c)). Resulting from spin-degeneracy, each \mathbf{k} value is assumed by two electrons. With the p_z electrons from each of the two basis atoms (A and B) the π or valence band is completely filled at $T = 0$, whereas the π^* or conduction band is empty. The Fermi level E_F intersects the π and π^* band exactly at the K-point, rendering it a semi-metal or zero-gap semiconductor, which can also be seen in the graphene density of states (Fig. 2.1 (d)). Fig. 2.1 (b) displays the roots of graphene's fame, which originates from its linear dispersing bands in the proximity of the K-point in reciprocal space, clearly distinguishing graphene from materials which feature a parabolic dispersion at the band edge.

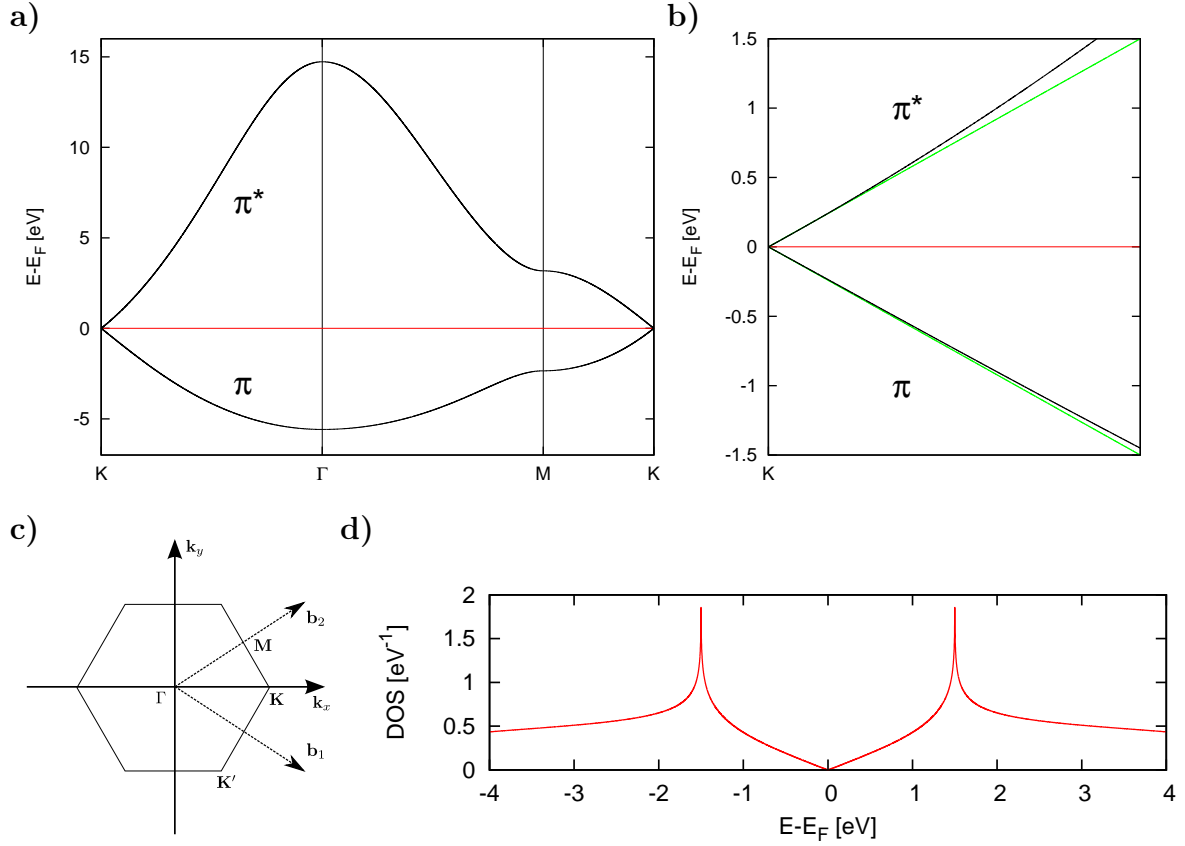


Figure 2.3: Tight-binding bandstructure of graphene's π - and π^* -bands. a) Bands along the closed path $K \rightarrow \Gamma \rightarrow M \rightarrow K$ in the first Brillouin zone. b) Linear dispersion of the valence and conduction bands in proximity to the K -point. The green lines indicate perfectly linear behavior. c) First Brillouin zone of graphene, including points of high symmetry. d) Density of states per unit cell as determined by Eq. (14) in Ref. [18].

2.2 Dirac fermions

A rather surprising consequence of graphene's linearly dispersing π bands close to the K -point is its connection to quantum electrodynamics (QED): due to their interaction with the periodic potential, new quasiparticles emerge at low energies E which are rather described as massless Dirac fermions [6, 5, 4]. This implies that the correct description of these particles has to move from the Schrodinger equation to the relativistic Dirac equation with an effective speed of light $v_F \approx 10^6 \text{ m s}^{-1}$, being described by the Dirac-like hamiltonian

$$\hat{H} = \hbar v_F \begin{pmatrix} 0 & k_x - ik_y \\ k_x + ik_y & 0 \end{pmatrix} = \hbar v_F \hat{\sigma} \mathbf{k}. \quad (2.22)$$

\mathbf{k} is the quasiparticle momentum, $\hat{\sigma}$ the 2D Pauli matrix and, as mentioned above, v_F corresponds to the speed of light. The conical shape of the bands at $E = E_F$ is

called Dirac cone and is caused by graphene's crystal symmetry, i.e. the two equivalent carbon sublattices A and B. These sublattices also necessitate the introduction of two-component wavefunctions, spinors, where each sublattice determines one component and is called pseudospin.

The charge carrier's relativistic behavior also enables experimentalists to probe some of the consequences of quantum electrodynamics. One of QED's most counter-intuitive predictions might probably be Klein's paradox, which states that relativistic particles are allowed to penetrate arbitrarily high and thick potential barriers with a transmission probability of 100% [21]. As opposed to particle physics, this very phenomenon can be realised experimentally much easier in condensed matter physics.

Chapter 3

Method

The main focus of the current thesis lies on the determination of the electronic and structural properties of graphene based solid state systems, a goal which we wish to accomplish by means of ab-initio quantum-mechanical simulations, i.e. calculations which, in the ideal case, solely rely on the system's Hamiltonian without the need for additional empirical data.

To be more precise, we employ the *Vienna Ab-initio Simulation Package* (VASP), developed by G. Kresse et al. [22, 23, 24]. The VASP code is based on Density Functional Theory (DFT), which represents an efficient way to numerically treat molecules and solids, i.e. quantum-mechanical many-body problems.

VASP makes use of pseudopotentials [25, 26] and a plane wave basis set to determine the ion electron interaction and to expand all cell periodic functions, respectively. For the valence states the pseudo-wave functions are replaced by true wavefunctions using the Projector Augmented Wave (PAW) formalism. Furthermore, VASP also allows for the calculation of forces and the full stress tensor for structure relaxation purposes. Several exchange-correlation potential approximations are implemented in the numerical code, ranging from LDA to different flavors of GGA.

In the following chapter, we wish to motivate and review some of the basic principles which are necessary when approaching quantum-mechanical many-body systems, starting by writing down the full Hamiltonian for N interacting electrons and M nuclei. Simplifications such as the Born-Oppenheimer approximation are employed to greatly facilitate the problem. Explicit methods for solving these system are presented next: for completeness and for historical reasons, we also want to shortly cover the Hartree equations and the more sophisticated Hartree-Fock equations. Finally, we give an overview of DFT since it forms the basis of the numerics incorporated in the program VASP.

If not denoted otherwise, the major content of the subsequent chapter is based on Refs. [27, 28, 29, 30, 31].

3.1 Born-Oppenheimer approximation

To obtain the electronic properties of a given material which consists of N electrons and M nuclei, one has to solve the system's Schroedinger equation,

$$\hat{H}\Psi(\mathbf{r}_1, \dots, \mathbf{r}_N, \mathbf{R}_1, \dots, \mathbf{R}_M) = E\Psi(\mathbf{r}_1, \dots, \mathbf{r}_N, \mathbf{R}_1, \dots, \mathbf{R}_M), \quad (3.1)$$

with \hat{H} being the multi-body Hamiltonian

$$\hat{H} = -\frac{1}{2} \sum_{i=1}^N \nabla_i^2 - \frac{1}{2} \sum_{I=1}^M \frac{\nabla_I^2}{n_I} + \frac{1}{2} \sum_{i=1}^N \sum_{j \neq i}^N \frac{1}{|\mathbf{r}_i - \mathbf{r}_j|} \quad (3.2)$$

$$+ \frac{1}{2} \sum_{I=1}^M \sum_{J \neq I}^M \frac{Z^2}{|\mathbf{R}_I - \mathbf{R}_J|} - \frac{1}{2} \sum_{i=1}^N \sum_{J=1}^M \frac{Z}{|\mathbf{r}_i - \mathbf{R}_J|}. \quad (3.3)$$

From Eq. (3.3), we identify the first (second) term with the kinetic energy of the electrons (nuclei), the third (fourth) term corresponds to the electrostatic electron-electron (nucleus-nucleus) repulsion and the last term represents the Coulombic electron-nucleus attraction. Note that we have employed atomic units ($m_e = e = \hbar = c = 1$), as well as adopted the notion that lower case letters (i,j) describe electrons and upper case letters (I,J) nuclei, respectively. The number n_I is determined by the ratio M_I/m_e .

This result, although seemingly simple, still makes it necessary to solve a system depending on $3N$ electronic and $3M$ ionic coordinates. It can, however, be simplified considerably by noticing that the nuclei's masses are much larger than their electronic counterparts. Keeping the nuclei's positions \mathbf{R}_I fixed and using their position as a parameter in further calculations, we arrive at the Born-Oppenheimer approximation [32], so that Eq. (3.3) now reads

$$\hat{H} = \underbrace{-\frac{1}{2} \sum_{i=1}^N \nabla_i^2}_{\hat{T}} + \underbrace{\frac{1}{2} \sum_{i=1}^N \sum_{j \neq i}^N \frac{1}{|\mathbf{r}_i - \mathbf{r}_j|}}_{\hat{V}_{ee}} - \underbrace{\frac{1}{2} \sum_{i=1}^N \sum_{J=1}^M \frac{Z}{|\mathbf{r}_i - \mathbf{R}_J|}}_{\hat{V}_{ext}} \quad (3.4)$$

$$= \hat{T} + \hat{V}_{ee} + \hat{V}_{ext}, \quad (3.5)$$

where \hat{T} is the electron's kinetic energy, \hat{V}_{ee} the Coulomb interaction between the N electrons and \hat{V}_{ext} labels the coulombic interaction of the electrons with the frozen nuclei, respectively. Here, the constant nucleus-nucleus interaction was neglected for convenience and has to be taken into account if one wishes to evaluate the system's total energy. \hat{T} and \hat{V}_{ee} are said to be universal since said expressions have this exact form in every N electron system. \hat{V}_{ext} , however, depends on the investigated material and is therefore characteristic for the actual system one is interested in.

3.2 Hartree and Hartree-Fock equations

Strategies to iteratively solve Schroedinger's equation for the many-body Hamiltonian in Eq. (3.5) lead to the Hartree-Fock equations and its predecessor, the Hartree equations. Both approaches make use of the variational principle to minimize the expectation value $\langle \Psi | \hat{H} | \Psi \rangle / \langle \Psi | \Psi \rangle$ of the system's Hamiltonian operator, however only the Hartree-Fock method accounts for the electron's fermionic character.

Hartree equation. Hartree's approach adopts the assumption that the wavefunction $|\Psi\rangle$ can be approximated by a product of independent single-electron orbitals $|\phi_i\rangle$,

$$|\Psi\rangle = \prod_i |\phi_i\rangle = |\phi_1\rangle \cdots |\phi_N\rangle. \quad (3.6)$$

Note that, since the spin degree of freedom is omitted in the Hartree approach, $|\Psi\rangle$ is not antisymmetric with respect to an exchange of particles. To minimize the system's energy, we write the expectation value as

$$\begin{aligned} E &= \frac{\langle \Psi | \hat{H} | \Psi \rangle}{\langle \Psi | \Psi \rangle} \\ &= \langle \phi_1 \cdots \phi_N | \hat{T} + \hat{V}_{ee} + \hat{V}_{ext} | \phi_1 \cdots \phi_N \rangle \end{aligned} \quad (3.7)$$

$$= \sum_i^N \langle \phi_i | \left(\hat{T} + \hat{V}_{ext} + \sum_{j \neq i} \langle \phi_j | \hat{V}_{ee} | \phi_j \rangle \right) | \phi_i \rangle. \quad (3.8)$$

This quantity is now varied with respect to $\langle \phi_i |$ such that the energy assumes an extremal value,

$$\frac{\delta}{\delta \langle \phi_i |} \left(\langle \Psi | \hat{H} | \Psi \rangle - \sum_i \epsilon_i \langle \phi_i | \phi_i \rangle \right) = 0. \quad (3.9)$$

Using ϵ_i as Lagrange multipliers the additional term $\sum_i \epsilon_i \langle \phi_i | \phi_i \rangle$ ensures that each one-electron wavefunction is normalized. We consequently obtain the Hartree equations,

$$\left\{ -\frac{1}{2} \nabla_i^2 + \hat{V}_{\text{eff}} \right\} |\phi_i\rangle = \epsilon_i |\phi_i\rangle, \quad (3.10)$$

$$\hat{V}_{\text{eff}} = \hat{V}_{ext} + \sum_{j \neq i} \langle \phi_j | \hat{V}_{ee} | \phi_j \rangle. \quad (3.11)$$

The resulting equations are therefore Schroedinger equations, where an electron i moves in an external potential originating from the ions, \hat{V}_{ext} , and an additional term which represents the electrostatic potential generated by all electrons $j \neq i$, $\sum_{j \neq i} \langle \phi_j | \hat{V}_{ee} | \phi_j \rangle$. This additional potential, also called the Hartree term, would arise from solving Poisson's equation using a charge density $\langle \phi_i | \phi_i \rangle$ for each electron.

Hartree-Fock equation. The product ansatz for the wavefunction $|\Psi\rangle$ does not take into account Pauli's principle which forbids two electrons sharing the same quantum-mechanical state. This deficiency can be cured by taking the wavefunction to be a Slater determinant, i.e. an antisymmetrized product function,

$$|\Psi\rangle = \frac{1}{\sqrt{N!}} \sum_P (-1)^P P \left\{ |\phi_1\rangle \cdots |\phi_N\rangle \right\} \quad (3.12)$$

$$= \frac{1}{\sqrt{N!}} \begin{vmatrix} |\phi_1(1)\rangle & \cdots & |\phi_1(N)\rangle \\ \vdots & \ddots & \vdots \\ |\phi_N(1)\rangle & \cdots & |\phi_N(N)\rangle \end{vmatrix}, \quad (3.13)$$

where the $|\phi_i(j)\rangle$ denotes an electron j occupying the orbital i . Plugging the antisymmetrized $|\Psi\rangle$ from Eq. (3.13) into the energy expectation value $\langle\Psi|\hat{H}|\Psi\rangle$ followed by a minimization yields

$$\begin{aligned} \left\{ -\frac{1}{2}\nabla_i^2 + \hat{V}_{\text{ext}} \right\} |\phi_i\rangle &+ \sum_j \langle\phi_j|\hat{V}_{ee}|\phi_j\rangle |\phi_i\rangle \\ &- \sum_j \langle\phi_j|\hat{V}_{ee}|\phi_i\rangle |\phi_j\rangle = \epsilon_i |\phi_i\rangle. \end{aligned} \quad (3.14)$$

The first three terms are obtained in analogy to the Hartree approach, while the additional energy term, $-\sum_j \langle\phi_j|\hat{V}_{ee}|\phi_i\rangle |\phi_j\rangle$, is called *exchange energy*. It becomes effective only for electrons which share the same spin, since $|\phi_i\rangle$ also includes the spin wavefunction which is orthogonal for spins of opposite direction. For electrons with different spin, the exchange energy is equal to zero. The exchange energy features a minus sign, thus *reducing* the energy for two electrons with equal spin. This behavior, which is an entirely quantum-mechanical effect which has no classical analogy, results from electrons with like spin avoiding each other, thus reducing their Coulomb energy. Note that, for $i = j$, the before divergent Hartree term is exactly canceled by the exchange term. The iteration of Eqn. (3.14) to obtain a self-consistent solution comes at a high computational cost, thus necessitating more elaborate methods to treat quantum-mechanical many-body systems.

3.3 Hohenberg-Kohn theorems and Kohn-Sham equations

Solving the Hamiltonian Eq. (3.5) poses severe difficulties due to its many-body nature, since even with the Born-Oppenheimer approximation the system's wavefunction

depends on $3N$ coordinates. In 1965, W. Kohn and L.J. Sham [33] proposed a new way to treat this multi-body problem by means of N coupled Schroedinger equations, describing a fictitious system of N non-interacting electrons. Incorporating the two theorems put forward by Hohenberg and Kohn [34],

Theorem 1

The electron density $n(\mathbf{r})$ uniquely determines the external potential \hat{V}_{ext} as well as the system's total energy, hence $E = E[n(\mathbf{r})]$

Theorem 2

The ground-state density $n_0(\mathbf{r})$ which yields $\int n_0(\mathbf{r})d\mathbf{r} = N$ minimizes the energy, $E_0[n_0(\mathbf{r})] = \min_{n(\mathbf{r})} E[n(\mathbf{r})]$

we express the energy as a functional of the electron density $n(\mathbf{r})$ rather than by means of the wavefunction $|\Psi\rangle$,

$$E[n(\mathbf{r})] = T[n(\mathbf{r})] + V_{ee}[n(\mathbf{r})] + V_{ext}[n(\mathbf{r})], \quad (3.15)$$

where the exact functional dependence is only known for $V_{ext}[n(\mathbf{r})]$, namely

$$V_{ext}[n(\mathbf{r})] = \int d\mathbf{r} n(\mathbf{r}) V_{ext}(\mathbf{r}). \quad (3.16)$$

W. Kohn and L.J. Sham [33] now rewrote Eq. (3.15) in terms of $T_s[n(\mathbf{r})]$, the kinetic energy of a virtual system of non-interacting electrons which yields the same density as the original interacting one, and the Hartree energy $U[n(\mathbf{r})]$, which stems from the electrostatic interaction of an electron with all other electrons, respectively,

$$U[n(\mathbf{r})] = \frac{1}{2} \int d\mathbf{r} \int d\mathbf{r}' \frac{n(\mathbf{r})n(\mathbf{r}')}{|\mathbf{r} - \mathbf{r}'|}, \quad (3.17)$$

$$T_s[n(\mathbf{r})] = -\frac{1}{2} \sum_{i=1}^N \int d\mathbf{r} \varphi_i^*(\mathbf{r}) \nabla^2 \varphi_i(\mathbf{r}). \quad (3.18)$$

Furthermore, the exchange-correlation energy $E_{xc}[n(\mathbf{r})]$ is introduced, accounting for both deviations of $T_s[n(\mathbf{r})]$ from the real kinetic energy $T[n(\mathbf{r})]$ as well as of $U[n(\mathbf{r})]$ from $V_{ee}[n(\mathbf{r})]$,

$$E_{xc}[n(\mathbf{r})] = \left(T[n(\mathbf{r})] - T_s[n(\mathbf{r})] \right) + \left(V_{ee}[n(\mathbf{r})] - U[n(\mathbf{r})] \right), \quad (3.19)$$

leading ultimately to

$$E[n(\mathbf{r})] = T_s[n(\mathbf{r})] + U[n(\mathbf{r})] + V_{ext}[n(\mathbf{r})] + E_{xc}[n(\mathbf{r})]. \quad (3.20)$$

We now minimize Eq. (3.20) with respect to the electron density $n(\mathbf{r})$, subject to the constraint that the total number of electrons is conserved,

$$0 = \frac{\delta}{\delta n(\mathbf{r})} \left\{ E[n(\mathbf{r})] - \mu \left(\int n(\mathbf{r}) d\mathbf{r} - N \right) \right\}. \quad (3.21)$$

Since the dependency of T_s on the density $n(\mathbf{r})$ is not known explicitly, we vary the wave functions φ_i^* and make use of the chain rule for terms which depend on $n(\mathbf{r})$,

$$0 = \frac{\delta T_s}{\delta \varphi_i^*} + \frac{\delta}{\delta n(\mathbf{r})} \left\{ U[n(\mathbf{r})] + V_{ext}[n(\mathbf{r})] + E_{xc}[n(\mathbf{r})] \right\} \frac{\delta n(\mathbf{r})}{\delta \varphi_i^*}. \quad (3.22)$$

Finally, this yields the famous Kohn-Sham equations,

$$\left\{ -\frac{1}{2} \nabla_i^2 + V_{\text{eff}}(\mathbf{r}) \right\} \varphi_i(\mathbf{r}) = \epsilon_i \varphi_i(\mathbf{r}), \quad (3.23)$$

with $i = 1, \dots, N$ and

$$n(\mathbf{r}) = \sum_{i=1}^N |\varphi_i(\mathbf{r})|^2, \quad (3.24)$$

$$V_{\text{eff}}(\mathbf{r}) = V_{\text{ext}}(\mathbf{r}) + \int \frac{n(\mathbf{r}')}{|\mathbf{r} - \mathbf{r}'|} d\mathbf{r}' + \frac{\delta E_{xc}(\mathbf{r})}{\delta n(\mathbf{r})}. \quad (3.25)$$

As is apparent from Eq. (3.23), we have now arrived at N coupled Schroedinger equations of non-interacting particles. The Kohn-Sham equations are now to be solved iteratively until self consistency is reached, starting from an initial guess $n^0(\mathbf{r})$ of the charge density. This guess is inserted into the effective potential $V_{\text{eff}}(\mathbf{r})$ which subsequently enables the solution of the Kohn-Sham equations Eqn. (3.23). The updated density $n(\mathbf{r})$ is obtained by summing over the square of the absolute values of the orbitals $\varphi_i(\mathbf{r})$. If the solution is not yet converged, i.e. the change of the density or energy from one iterative step to the next is still larger than a certain pre-defined threshold, one re-evaluates the effective potential at the density $n(\mathbf{r})$ and repeats. Fig. 3.1 illustrates this iterative procedure to solve the Kohn-Sham equations with the help of a flow chart.

Note that we have yet to put forward the expression for the exchange correlation energy $E_{xc}[n(\mathbf{r})]$. Under the hypothetic assumption that one knew the exact functional form of this expression, one could solve the ground-state properties for the interacting

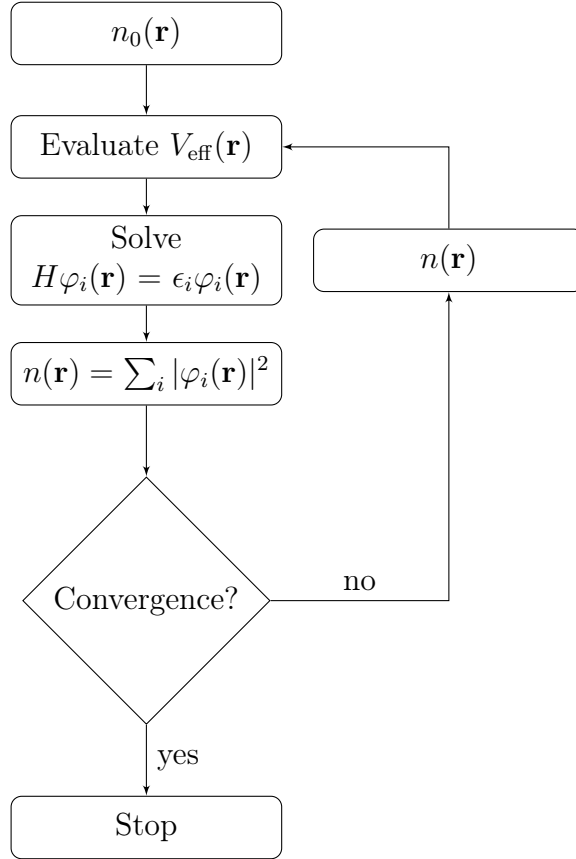


Figure 3.1: Flow chart illustrating the procedure to solve Eq. (3.23), as presented in Ref. [31].

system exactly. This quantity is, however, not known and thus has to be approximated in practice. Numerically there exist several approximations of the exchange correlation term, for which we want to give a brief overview in the following.

3.4 Exchange-correlation functionals

The sole unknown expression which is required to be able to solve the Kohn-Sham equations Eq. (3.23) and which is therefore subject to approximations is the unknown exchange-correlation potential $v_{xc}(\mathbf{r})$,

$$v_{xc}(\mathbf{r}) = \frac{\delta E_{xc}(\mathbf{r})}{\delta n(\mathbf{r})}. \quad (3.26)$$

LDA. In the local density approximation (LDA), $E_{xc}(\mathbf{r})$ is approximated by a exchange-correlation potential which is local in space,

$$E_{xc}^{LDA}[n(\mathbf{r})] = \int \epsilon_{xc}(n(\mathbf{r}))n(\mathbf{r}) \, d\mathbf{r}. \quad (3.27)$$

The quantity $\epsilon_{xc}(n(\mathbf{r}))$ represents the exchange-correlation energy density as obtained from a homogeneous electron gas.

GGA. More elaborate functionals also take gradient contributions of the electron density into account, resulting in the generalized gradient approximations (GGA) [35],

$$E_{xc}^{GGA}[n(\mathbf{r})] = \int f(n(\mathbf{r}), |\nabla n(\mathbf{r})|) n(\mathbf{r}) d\mathbf{r}, \quad (3.28)$$

which exists in a multitude of different parametrizations.

Above expressions can be refined even further, by considering spin up and spin down densities separately, leading to the local spin density approximation (LSDA),

$$E_{xc}^{LSDA}[n_{\uparrow}(\mathbf{r}), n_{\downarrow}(\mathbf{r})] = \int \epsilon_{xc}(n_{\uparrow}(\mathbf{r}), n_{\downarrow}(\mathbf{r})) n(\mathbf{r}) d\mathbf{r}, \quad (3.29)$$

and

$$E_{xc}^{GGA}[n_{\uparrow}(\mathbf{r}), n_{\downarrow}(\mathbf{r})] = \int f(n_{\uparrow}(\mathbf{r}), n_{\downarrow}(\mathbf{r}), \nabla n_{\uparrow}(\mathbf{r}), \nabla n_{\downarrow}(\mathbf{r})) n(\mathbf{r}) d\mathbf{r}, \quad (3.30)$$

with $n(\mathbf{r}) = n_{\uparrow}(\mathbf{r}) + n_{\downarrow}(\mathbf{r})$.

In the course of this thesis, we exclusively employ spin-polarized calculations. Both the local density approximation (LDA) and the GGA in the Perdew-Burke-Ernzerhof (PBE) [36] parametrization are used as exchange-correlation functionals.

3.5 Van-der-Waals interaction

Above functionals are successful if applied to systems which form by means of covalent or ionic bonds, i.e. where chemical bonds are present. They give, however, poor results in weakly bonded systems, such as graphite, molecular crystals, organic compounds, molecules adsorbed on surfaces and, also, graphene adsorbed on metals. This failure stems from the fact that LDA and GGA don't include nonlocal dispersive forces, such as van-der-Waals (vdW) forces [37, 38, 39, 40]. In the following we want to introduce shortly the underlying physics.

3.5.1 Background

The van-der-Waals or dispersion force is a long-ranged interaction acting between neutral atoms. Even though these systems do not possess a permanent dipole moment,

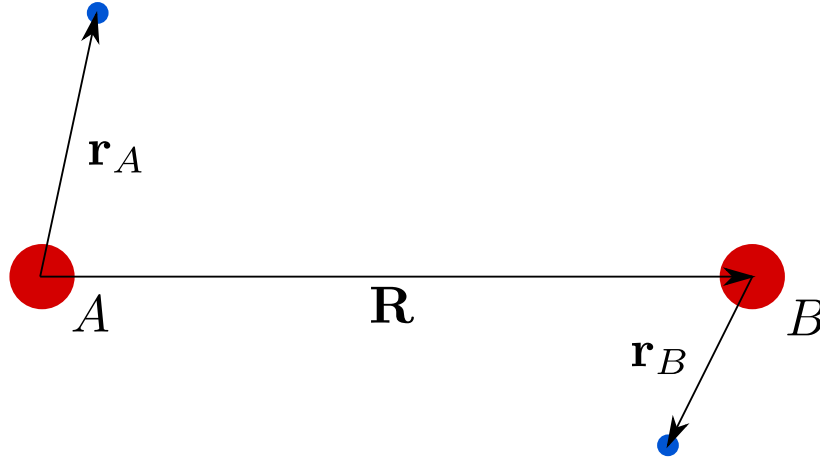


Figure 3.2: Two hydrogen atoms A and B, well separated by a distance $\mathbf{R} \gg \mathbf{r}_A, \mathbf{r}_B$. The coordinate \mathbf{r}_i correspond to the vectors pointing from the protons to the adjacent electrons.

fluctuations of the electron cloud around the nucleus develop temporary dipoles that result in an electric field which induces dipoles in nearby atoms by polarization.

To make this more quantitative, consider, e.g., two hydrogen atoms which are spatially well separated, in analogy to the treatment in Ref. [41]. The system is described by the Hamiltonian H ,

$$\begin{aligned}
 H = & -\frac{1}{2}\nabla_A^2 - \frac{1}{r_A} - \frac{1}{2}\nabla_B^2 - \frac{1}{r_B} \\
 & + \frac{1}{R} + \frac{1}{|\mathbf{R} + \mathbf{r}_B - \mathbf{r}_A|} - \frac{1}{|\mathbf{R} - \mathbf{r}_A|} - \frac{1}{|\mathbf{R} + \mathbf{r}_B|}.
 \end{aligned} \tag{3.31}$$

See Fig. 3.2 for an explanation of the coordinates employed. The first line of Eq. (3.31) corresponds to twice the Hamiltonian of an isolated hydrogen atom, $H_0 = H_0^A + H_0^B$. The second line describes the residual interaction W which is small for large separations \mathbf{R} and can thus be approached with perturbation theory. We choose the wavefunction $\Psi_0(\mathbf{r}_A, \mathbf{r}_B)$ as a product of hydrogen's groundstate wavefunctions $\varphi_i(\mathbf{r}_i)$,

$$\Psi_0(\mathbf{r}_A, \mathbf{r}_B) = \varphi_A(\mathbf{r}_A)\varphi_B(\mathbf{r}_B), \tag{3.32}$$

$$H_0^i \varphi_i(\mathbf{r}_i) = \varepsilon_0 \varphi_i(\mathbf{r}_i), \tag{3.33}$$

where i denotes the atomic site and ε_0 the energy eigenvalue of hydrogen's groundstate. To obtain the eigenvalue E_0 , we act with H_0 on the wavefunction $\Psi_0(\mathbf{r}_A, \mathbf{r}_B)$,

$$H_0 \Psi_0(\mathbf{r}_A, \mathbf{r}_B) = E_0 \Psi_0(\mathbf{r}_A, \mathbf{r}_B), \tag{3.34}$$

resulting in $E_0 = 2\varepsilon_0 < 0$. We now rewrite the interaction term W by choosing our

coordinate system such that the z-axis connects both hydrogen atoms, i.e. $\mathbf{R} = R \mathbf{e}_z$, yielding

$$W = \frac{1}{R} + \frac{1}{\sqrt{R^2 + 2\mathbf{R} \cdot (\mathbf{r}_B - \mathbf{r}_A) + (\mathbf{r}_B - \mathbf{r}_A)^2}} - \frac{1}{\sqrt{R^2 + 2\mathbf{R} \cdot \mathbf{r}_B + r_B^2}} - \frac{1}{\sqrt{R^2 - 2\mathbf{R} \cdot \mathbf{r}_A + r_A^2}} \quad (3.35)$$

$$= \frac{1}{R} \left(1 + \frac{1}{\sqrt{1 + 2\frac{(z_B - z_A)}{R} + \frac{(\mathbf{r}_B - \mathbf{r}_A)^2}{R^2}}} - \frac{1}{\sqrt{1 + 2\frac{z_B}{R} + \frac{r_B^2}{R^2}}} - \frac{1}{\sqrt{1 - 2\frac{z_A}{R} + \frac{r_A^2}{R^2}}} \right) \quad (3.36)$$

Expanding the $(1 + x)^{-1/2}$ expression to third order we obtain, after some manipulations,

$$W \approx \frac{1}{R^3} \left(\mathbf{r}_A \cdot \mathbf{r}_B - 3 \left(\mathbf{r}_A \cdot \hat{\mathbf{R}} \right) \left(\mathbf{r}_B \cdot \hat{\mathbf{R}} \right) \right), \quad (3.37)$$

which is the interaction between two dipoles separated by a distance R . Note that we use atomic units, therefore the atom's dipole moment is simply given by \mathbf{r}_i . $\hat{\mathbf{R}}$ corresponds to the unit vector pointing in the direction of \mathbf{R} .

To first order the energy correction vanishes because the groundstate wavefunction of hydrogen is spherically symmetric, i.e. $\Delta E^{(1)} = \langle \Psi_0 | W | \Psi_0 \rangle = 0$. By means of second order perturbation theory, the second order energy correction is given by

$$\Delta E^{(2)} = \sum_{n \neq 0} \frac{|\langle \psi_n | W | \psi_0 \rangle|^2}{E_0 - E_n}. \quad (3.38)$$

Here, $|\Psi_n\rangle = |\varphi_{An}\rangle |\varphi_{Bn}\rangle$ denotes the electron's excited states and E_n their corresponding eigenvalue. Plugging Eq. (3.37) into above equation, we thus arrive at the famous van-der-Waals interaction term,

$$\Delta E_{vdW} \propto -\frac{1}{R^6}, \quad (3.39)$$

which leads to a lowering in energy and is thus an attractive force. Note that the interaction goes with R^{-6} . The vdW force mainly contributes to the interaction between neutral atoms but also exists for charged ions. In this case, however, the monopole contribution of the Coulomb interaction dominates.

3.5.2 Implementation

Since the incorporation of the nonlocal electron-electron correlations into DFT is not straightforward and a challenging task, several approaches are followed to account for the vdW interaction.

Grimme corrections. In Ref. [40], S. Grimme approached the missing nonlocal and long-ranged correlation effects in GGA functionals by including a modified version of the empirical dispersion correction E_{disp} to the Kohn-Sham energy $E_{\text{KS-DFT}}$ as introduced in Ref. [42],

$$E_{\text{DFT-D}} = E_{\text{KS-DFT}} + E_{\text{disp}} \quad (3.40)$$

with

$$E_{\text{disp}} = -s_6 \sum_{i=1}^{N-1} \sum_{j=i+1}^N \frac{C_6^{ij}}{R_{ij}^6} f_{\text{dmp}}(R_{ij}). \quad (3.41)$$

N is the number of atoms in the system, C_6^{ij} corresponds to the dispersion coefficient for an atom pair ij , s_6 is a global scaling factor dependent on the employed functional and R_{ij} is the interatomic distance. f_{dmp} is a damping function which ensures that near-singularities for small R are avoided. Our calculations utilize the Perdew-Burke-Ernzerhof functional including the above force-field corrections, referred to as PBE+Grimme in the following.

vdW-DF. In vdW-DF and its refinements [43, 38], the exchange-correlation energy is written as

$$E_{xc} = E_x^{\text{GGA}} + E_c^{\text{LDA}} + E_c^{\text{nl}}, \quad (3.42)$$

where E_x^{GGA} is the GGA exchange energy, E_c^{LDA} the local correlation energy as obtained within LDA and E_c^{nl} accounts for the nonlocal part. In its simplest form, this quantity is given by

$$E_c^{\text{nl}} = \frac{1}{2} \int d^3\mathbf{r} \int d^3\mathbf{r}' n(\mathbf{r}) \phi(\mathbf{r}, \mathbf{r}') n(\mathbf{r}'), \quad (3.43)$$

where the function $\phi(\mathbf{r}, \mathbf{r}')$ is a function depending on $\mathbf{r} - \mathbf{r}'$ and the densities n in the proximity of \mathbf{r} and \mathbf{r}' , respectively. In the present work, the functional optB88 was employed [38, 39], which functional has only recently been implemented into VASP.

Chapter 4

Results

If placed on a metal substrate like, e.g., Nickel, Ruthenium or Rhodium, graphene couples strongly to its support, which consecutively leads to the destruction of graphene's unique and favorable electronic structure. Most importantly, its linear dispersion near the Dirac point is lost. With regard to potential future graphene based electronic devices, which benefit exactly from this feature, it is therefore desirable to overcome this shortcoming by tailoring the electronic structure of these systems.

As current research demonstrates, this can indeed be accomplished by the incorporation of an additional layer of a noble metal between the substrate and the graphene sheet. This layer is more or less seen as a spacer layer which leads to a reduced overlap of the involved graphene and metal orbitals and should thus help the graphene states to regain their freestanding, ideal behavior [12, 13, 14].

Controlling the intercalation process is fundamental if one wishes to effectively achieve this decoupling. The exact underlying mechanisms are, however, not yet fully understood and still subject to current investigations. In Ref. [44], e.g., the formation of intercalated nanoislands (INIs) of Ni is traced back to two main contributions: the diffusion through pre-existing lattice defects in graphene and via metal-generated defects followed by defect healing of the graphene lattice. The second mechanism is based on the observation that some INIs do not exhibit any perturbations of their moiré structure, as for example shown in Fig. 4.1.

In the following, we thus want to assess the question of *how* intercalated layers are formed under Gr/Ir(111) by determining the energy barriers a single nickel atom encounters during the intercalation process.

In the second part of this chapter, we will analyze the consequences of intercalation for Gr/Ag/Re, which already features an additional intercalated monolayer of Ag. Here we have experimental angle-resolved photoemission spectroscopy (ARPES) data at hand which were provided by M. Papagno et al. [45]. Contrary to expectations, these measurements did not reveal a behavior known for similar systems, but show a

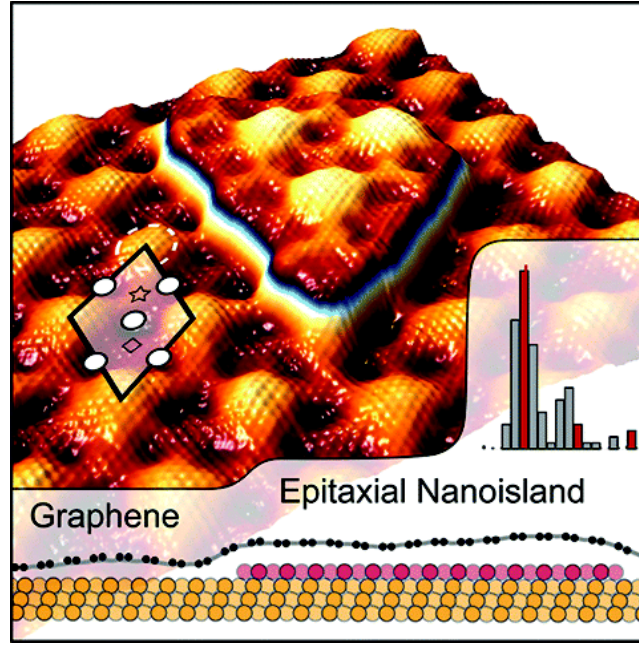


Figure 4.1: STM image of an intercalated Ni island underneath Gr/Ir(111) as found in experiment. The inset at the bottom sketches the fact that islands can also be found underneath areas of unmodified graphene sheets. This figure was taken from Ref. [44].

not at all negligible residual coupling.

4.1 Intercalation process: Graphene/Ni/Ir(111)

4.1.1 Introduction

Understanding the formation of a layer of foreign atoms between graphene and its supporting substrate by the process of intercalation plays an important role in experimentally controlling the growth of intermediate layers and in assessing experimental data. This knowledge can then, e.g., put into action to efficiently reduce the coupling of strongly interacting graphene/metal systems, as will be shown in the subsequent section.

In a first step towards intercalation in experiment, epitaxial graphene is grown on the surface, e.g., by exposure to hydrocarbons. Subsequent heating leads to cracking and a desorption of the hydrogen atoms [18]. The hereby grown graphene sheet is then covered with the desired material to initiate intercalation. This is followed by an annealing procedure of defined time and temperature. Fig. 4.2 illustrates this schematically. Note that the intercalation process happens *after* graphene is already present on the surface.

The rates of the various reaction processes occurring experimentally depend, firstly,

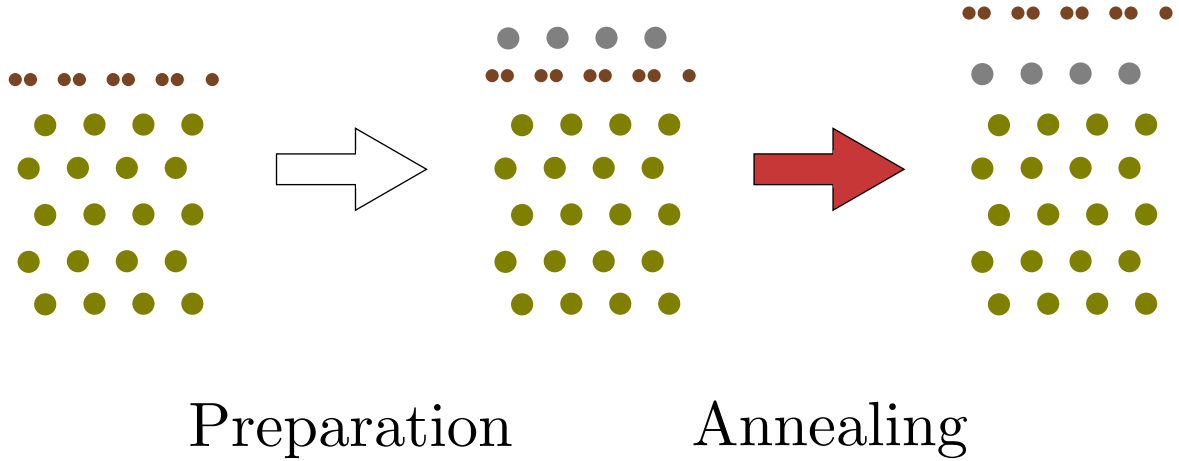


Figure 4.2: Schematic illustration of the experimental annealing process to achieve intercalation. In the first step graphene is grown on the surface. The foreign atoms are then positioned on top of the Gr/metal system, followed by annealing. During the heat exposure intercalation occurs by atoms diffusing through the graphene sheet.

on the applied temperature during the annealing and can thus be controlled by the experimenter. The second key quantity is the height of the energy barriers the intercalating atoms feel during the intercalation process, which we will analyze below for the specific system Gr/Ir(111).

4.1.2 Numerics

In what follows, we want to numerically investigate the intercalation paths which lead to the formation of a Ni layer under Gr/Ir(111). To achieve this, the energy barriers a single Ni atom encounters when diffusing through graphene are determined. We start out by investigating the diffusion while completely neglecting the supporting substrate. Once the transition mechanism is obtained, we will use the transition state structure to evaluate the full, supported system, thus including the Ir(111) substrate in our calculations.

4.1.2.1 Setup

Throughout the subsequent computations, we make use of the DFT code VASP [24, 22]. As mentioned in chapter 3, we allow for a spin-polarized calculation. PAW potentials [25, 26] and a cutoff-energy of 400 eV are employed. All numerical runs were performed in a 4×4 cell, except where explicitly noted. We used the local density approximation (LDA) to approximate the exchange-correlation energy and the Γ -only version of VASP, i.e. a $1 \times 1 \times 1$ grid to numerically sample the Brillouin zone.

The structural properties of the graphene layer were taken from the data shown in the next section of this chapter.

4.1.2.2 Methods

To determine the reaction barrier of the diffusing Ni atom, we adopt two strategies. To obtain a good guess of the reaction mechanism, we search at first for the transition state more or less by hand, a procedure we term *fixed coordinate method*. Based on the output of this search, a more refined search algorithm is used, given by the *dimer method* which we will review subsequently.

Fixed coordinate method. In a more or less brute force attempt, we reduce the z-distance of the Ni atom relative to the graphene layer gradually, employing a fixed step-size (Fig. 4.3). At each distance, we determine the system's total energy after allowing the most nearby carbon atoms of the graphene sheet to relax until all forces are smaller or equal than a threshold of $0.01 \text{ eV}/\text{\AA}$. The atoms constituting the boundary of the cell are kept fixed in this process. Hints at the involved reaction mechanism are obtained from the recorded energy vs. reaction coordinate data, which is, in the present case, just the z-distance between Ni and the initial z-coordinate of the graphene sheet. This method will, in the following, also be referred to as the *fixed coordinate approach*.

Dimer method. The above method allows an approximate guess of the correct transition state (TS), which state represents a saddle point on the potential energy

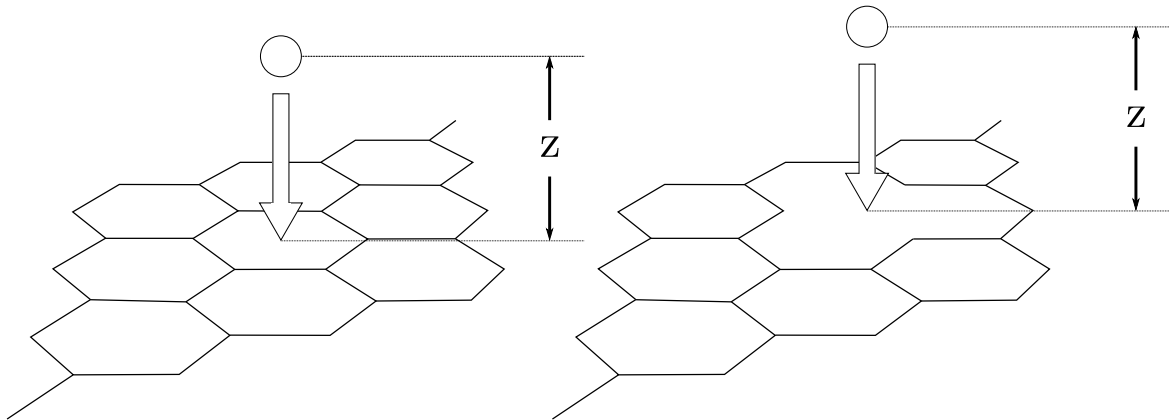


Figure 4.3: Sketch of the fixed coordinate method, as employed in our numerics. The z-distance of the diffusing atom is decreased gradually. We show here two examples of the fixed coordinate approach in a 4×4 unit cell, i.e. the diffusion through a pristine graphene sheet (left) and through a vacant site in the graphene layer (right), respectively. For simplicity the cell is depicted using a wireframe representation.

surface (PES). Directly at the TS, the forces which act on the Ni atom are equal to zero. Since, however, the actual transition state can differ quite significantly from the one obtained by the fixed coordinate method, a more refined algorithm for finding the saddle point is needed. One efficient approach to accomplish this is the dimer method [46, 47] and, as implemented into VASP, the improved dimer method [48]. Unlike conventional techniques, the dimer method embodies a mode-following method which only requires the first derivatives of the energy, rendering it also capable of treating large systems. Technically, the dimer method uses two replicas of the system, thus lending this technique its name. The dimer is used to transform the forces such that the system converges towards a saddle point rather than a minimum by means of an optimization procedure allowing both a translation and a rotation of the dimer [47].

The implementation of this procedure into VASP is not as straight-forward as before. Following the suggestions from the VASP manual on the application of the dimer method¹, three steps are required to determine the energy diagram and, hence, the energy barrier. Starting from the TS guess, we calculate the frequency spectrum of the system. The mode featuring an imaginary frequency is then used as an initial dimer axis in the actual dimer method run. A sampling of the PES is achieved by iterative rotation and translation of the dimer. If converging, the dimer should move towards the energy maximum of the reaction path which forms a saddle point. Convergence is achieved if the forces on the ions, which were allowed to move, are smaller than 0.03 eV/Å. To obtain the energies of the initial (IS) and final state (FS), we deflect the Ni atom from its (unstable) equilibrium position and relax the system by means of a velocity quenched algorithm as implemented in VASP by setting `IBRION=3`. The energy and positional data is extracted from the `OSZICAR` and `XDATCAR` output files. In the appendix we include the scripts which were written during this thesis to accomplish the above mentioned task.

In contrast to the fixed coordinate approach, where the reaction coordinate is determined by the Ni atom's z-coordinate, we introduce here another measure based on the norm between two different configurations $\xi^{(i)}$ belonging to consecutive iterative steps in the ionic relaxation process,

$$d = \sum_i |\xi^{(i+1)} - \xi^{(i)}| , \quad (4.1)$$

where the index i runs over all ionic iteration steps. The system's structure is entirely specified by the 3N dimensional configuration vector $\xi^{(i)}$, with N denoting the total

¹<http://cms.mpi.univie.ac.at/vasp/vasp/vasp.html>

number of ions in the employed unit cell,

$$\xi^{(i)} = \begin{pmatrix} \mathbf{R}_1^{(i)} \\ \vdots \\ \mathbf{R}_N^{(i)} \end{pmatrix}. \quad (4.2)$$

4.1.2.3 Unsupported graphene

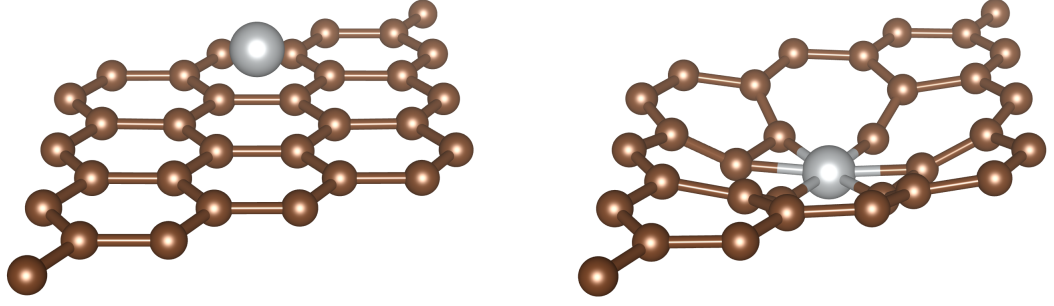
Pristine graphene sheet. Fig. 4.4 shows the results of the diffusion of a Ni atom through the central graphene ring in a p(4x4) cell for both, the fixed coordinate as well as the dimer method. Of the 32 carbon atoms, we fix the outermost ions and allow the inner C atoms to move in all directions during relaxation. We present the structures for the initial and transition state in (a) and the total energy of the unit cell [eV] versus the reaction coordinate [\AA] in (b). In the left panel of the bottom row, we show the results as obtained by the fixed coordinate method. We start the search for the transition state at a z-distance of 7.5 \AA between the graphene sheet and the Ni atom, which lies exactly in the middle of our 15 \AA thick vacuum region. Here, we use the convention that the initial state lies to the left, featuring negative values of the reaction coordinate. Note that the zero point in our fixed coordinate calculations does not correspond to the transition state. Since the closest carbon atoms are allowed to give way when the Ni atom approaches, the transition state can be found about 1 \AA below the initial position of the graphene sheet.

The $d = 7.5$ \AA configuration lies about 2.64 eV above the reactant state energy, which was chosen as the reference energy state. It corresponds to the minimum at about -1.5 \AA . Upon approaching, the Ni atom is caught in a local minimum basin. For the intercalation of Ni to happen, i.e. to get from the initial state on the left of the barrier to the final state on the right, an energy barrier of 11.95 eV has to be overcome. Approximately 12 eV is a very large barrier and is unlikely to be overcome at typical annealing temperatures.

Note that our curve features a discontinuous jump at the TS. This is an artefact of the procedure which we employ: due to the constant step size the evading carbon atoms are suddenly confronted with a repellent force as soon as the Ni atom moves over the transition state. A smoother behavior in the energy vs. reaction coordinate plots will be obtained by the dimer method in the following.

The right panel of (b) in Fig. 4.4 corresponds to the data as acquired by the dimer method, starting from the configuration closest to the TS based on the fixed coordinate approach. The diffusion barrier determined by this method differs by only 30 meV from the previously obtained data. The marginal difference therefore does not change the above assessment of the probability of this particular type of reaction.

a)



b)

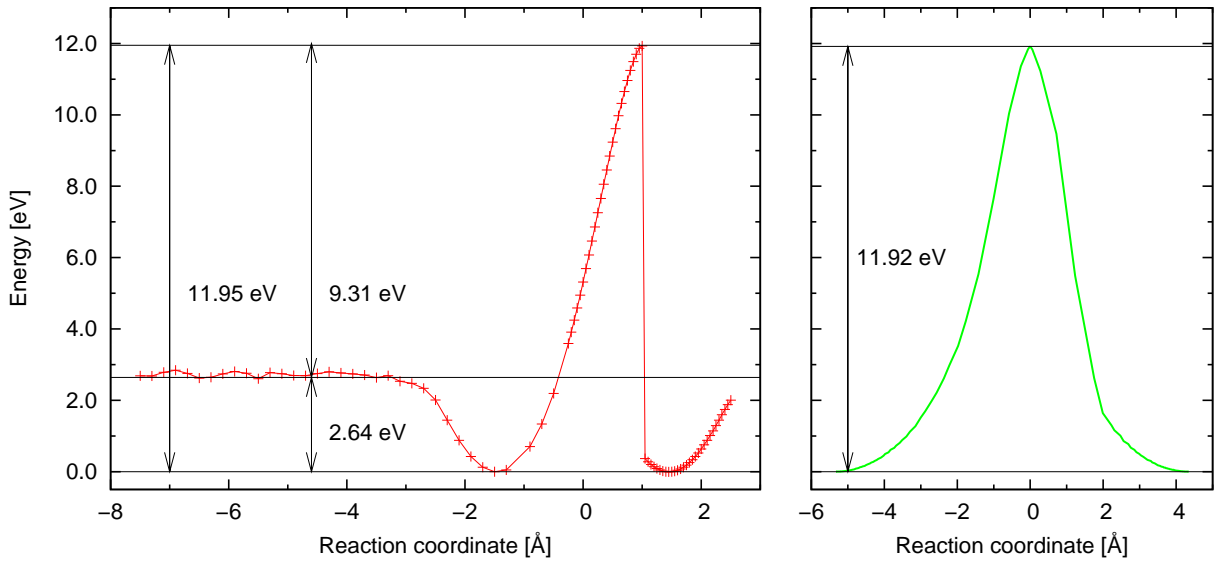
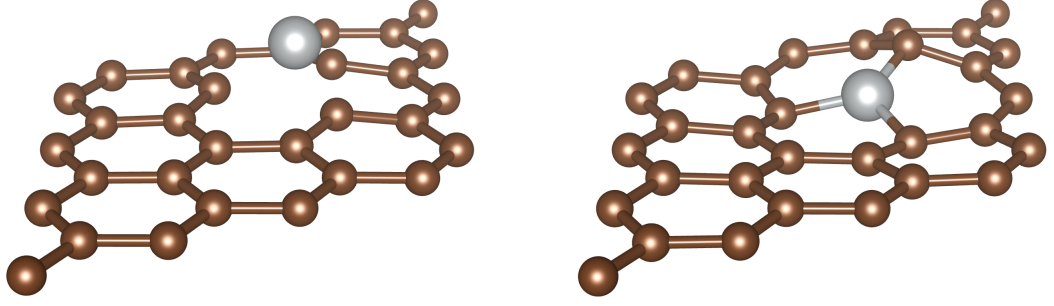


Figure 4.4: a) Structures of the $p(4 \times 4)$ cell at the initial (left) and transition state (right). b) Total energy of the unit cell [eV] as a function of the reaction coordinate [Å], shifted to feature the initial state as the reference energy. The unit cell consists of 32 carbon atoms and one Ni atom, respectively. For the fixed coordinate model (left panel), black lines are included which correspond to the transition state and the $d = 7.5$ Å configuration. The right panel displays the barrier as obtained by the dimer method. Note that both approaches use different definitions of the reaction coordinate, the x-coordinates are therefore not to scale (see text for details).

An explanation of this finding might most presumably be the fact that we already had a very good initial guess of the transition mechanism when we employed the fixed coordinate method.

Defective graphene sheet. The above obtained energy barriers are too high to explain the formation of intercalated Ni layers as observed by experiment [44]. Another possibility which we now want to analyze is the reaction happening at a vacant carbon

a)



b)

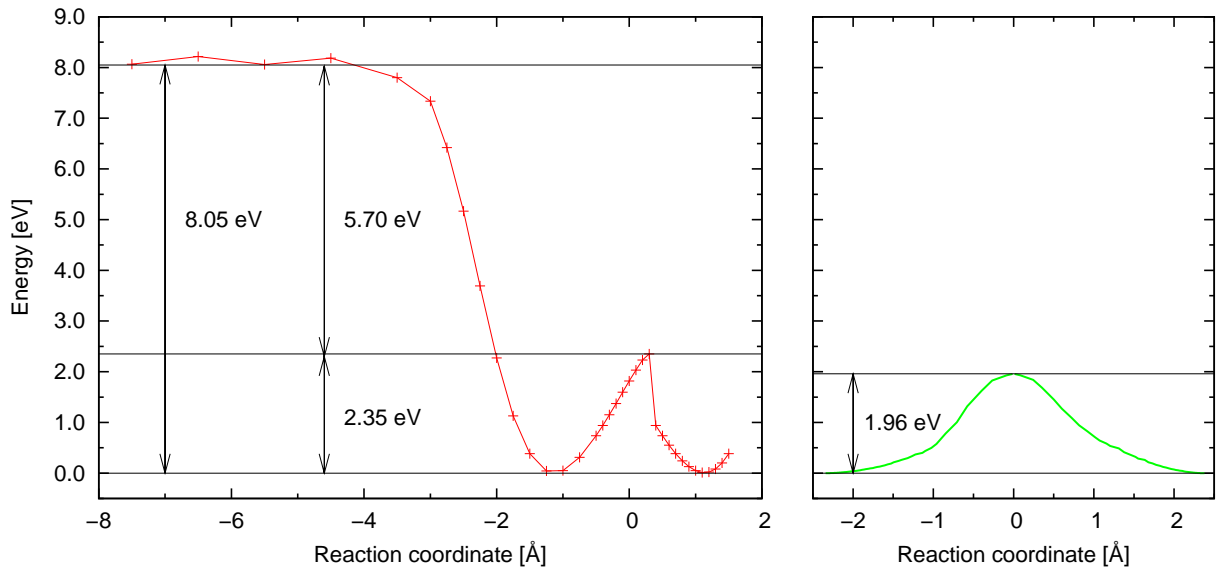
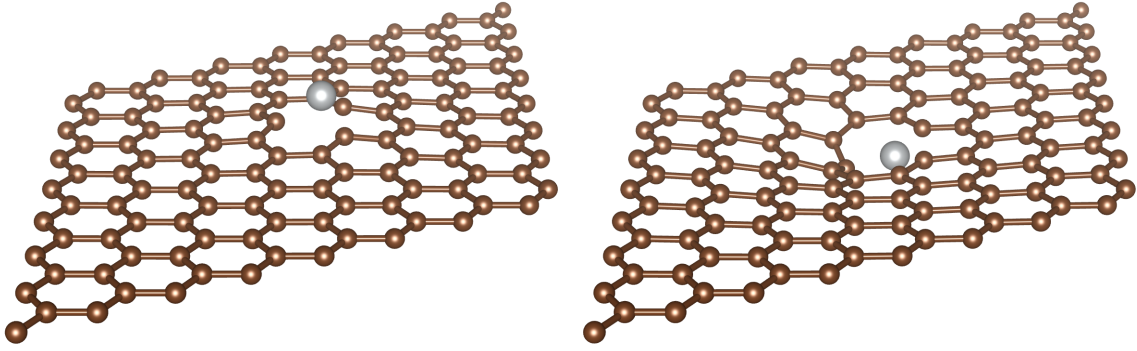


Figure 4.5: a) Structures of the $p(4 \times 4)$ cell at the initial (left) and transition state (right). b) Total energy of the unit cell [eV] as a function of the reaction coordinate [\AA], shifted to feature the initial state as the reference energy. The unit cell consists of 31 carbon atoms and one Ni atom, respectively. For the fixed coordinate model (left panel), black lines are included which correspond to the transition state and the $d = 7.5 \text{ \AA}$ configuration. The right panel displays the barrier as obtained by the dimer method. Note that both approaches use different definitions of the reaction coordinate, the x-coordinates are therefore not to scale (see text for details).

site in the honeycomb lattice, see (a) in Fig. 4.5. Qualitatively speaking, it is obvious that a defect will be more reactive than a pristine graphene ring. In the following we want to make this assertion more quantitative.

Part (b) of Fig. 4.5 depicts the data in analogy to our treatment of the pristine graphene system. Comparing the energy diagrams, we now have a rather different picture than before. Approaching the graphene surface, the Ni atom gains 8.05 eV on its way to the reactant state in the minimum at about -1.1 \AA . This portion of

a)



b)

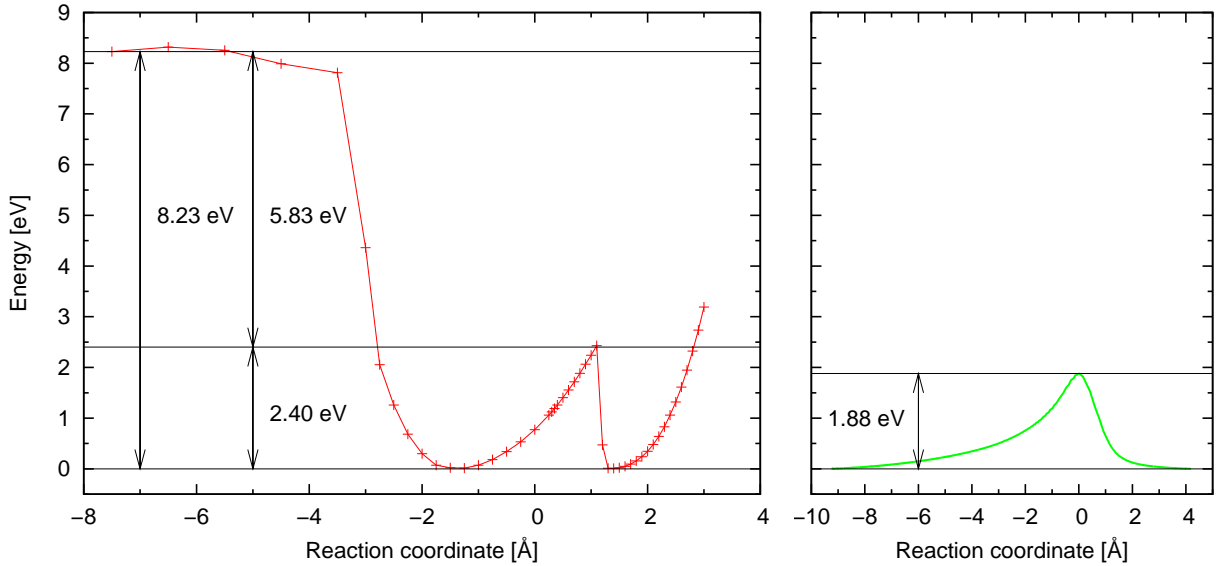


Figure 4.6: a) Structures of the p(8x8) cell at the initial (left) and transition state (right). b) Total energy of the unit cell [eV] as a function of the reaction coordinate [Å], shifted to feature the initial state as the reference energy. The unit cell consists of 127 carbon atoms and one Ni atom, respectively. For the fixed coordinate model (left panel), black lines are included which correspond to the transition state and the $d = 7.5$ Å configuration. The right panel displays the barrier as obtained by the dimer method. Note that both approaches use different definitions of the reaction coordinate, the x-coordinates are therefore not to scale (see text for details).

energy corresponds to the large vacancy energy of graphene and is a consequence of the strong bonding of graphene's carbon atoms. Most evidently, the energy barrier is significantly reduced by almost 10 eV, resulting in a diffusion barrier of 2.35 eV. A treatment which takes the TS as determined in the fixed coordinate run and employs the dimer method yields, finally, 1.96 eV, which is a by 0.39 eV smaller barrier. This

result represents a much more likely mechanism for intercalation.

Since the next nearest-neighbors of the diffusing Ni atom in our p(4x4) cell are already fixed, we also checked if this restriction leads to any substantial deviations by examining a p(8x8) cell (see Fig. 4.6). Both the fixed coordinate and dimer method were employed for this system. Difficulties arose during the dimer run, where we encountered a failure of VASP to converge the system towards the saddle point and resulted in the ions scattering in all directions. Fortunately, this behavior could be counteracted by manually setting the VASP flags `STEP_SIZE` and `STEP_MAX`, which flags both control step sizes for the dimer optimization steps, to 80% of its default values. The results obtained in this larger cell are, as expected, similar to the ones obtained in the smaller p(4x4) cell. For the fixed coordinate method the values differ from the p(4x4) cell by about 2%. By means of the dimer method we get, for an optimized transition state geometry, deviations of approximately -4% compared to the smaller cell's barrier. We can thus conclude that the p(4x4) cell already represents a large enough system. We might add that the lowering of the barrier stems from the fact that the larger 8x8 supercell offers more degrees of freedom for the ionic relaxation.

We still have, however, to consider the full system, i.e. Gr/Ir(111), which we will examine in the following section.

4.1.2.4 Supported graphene

The transition state structure, as obtained by the dimer method for the p(4x4) cell featuring a vacancy, was then put on a three layered Ir(111) slab in the top-fcc arrangement, i.e. one C atom on top of Ir and the other on the fcc hollow site. This interface structure offers therefore two options for a vacancy. In this work, however, we focus on a defect directly above the top site. To achieve an epitaxial graphene layer, the substrate was compressed by about 10% so that the iridium support matches the lattice structure of the terminating graphene sheet. The spacing between the fixed carbon atoms and the substrate was determined such that we examined the equilibrium distance between an ideal graphene sheet and the Ir(111) surface in an energy vs. graphene-substrate distance scan analogous to the treatment in the next part of this chapter, leading to $d = 3.1 \text{ \AA}$. For the dimer run, the substrate ions were kept fixed while the inner carbon atoms were again allowed to move in all directions.

Fig. 4.7 summarizes our findings. To the left, at -3.5 \AA , we have the reactant state which serves as a reference energy in our calculations. Surmounting the energy barrier would require 1.50 eV, which is a significant reduction of the barrier compared to the unsupported system. Additionally, the Ni atom is stabilized at the final (=intercalated) state, differing by 1.08 eV from the initial state. Fig. 4.8 provides the structures as

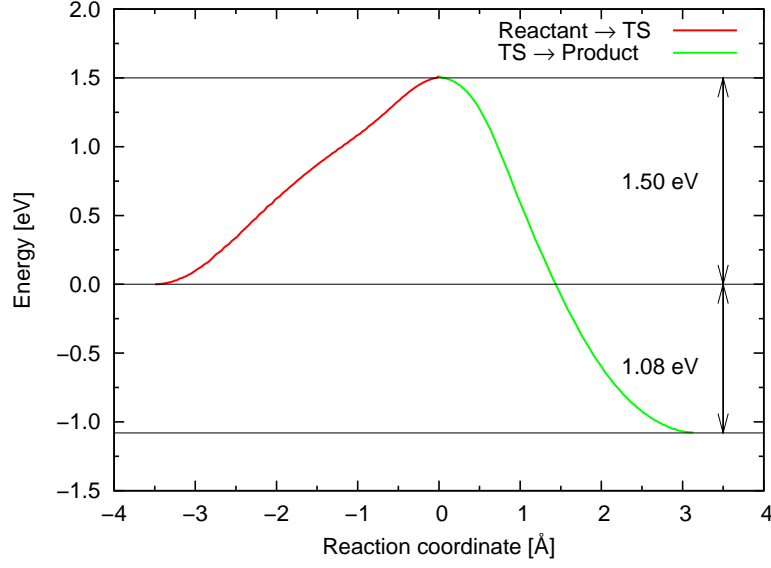
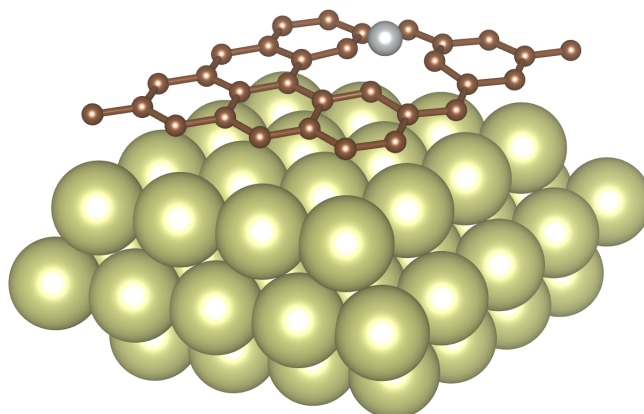


Figure 4.7: Total energy of the unit cell [eV] as a function of the reaction coordinate [Å] as obtained by the dimer method, shifted to feature the initial state as the reference energy. The unit cell consists of 48 Ir atoms, 31 carbon atoms and one Ni atom. Black lines are included which correspond to the initial state (at 0.0 eV), transition state (at 1.50 eV) and the final state (-1.08 eV), respectively.

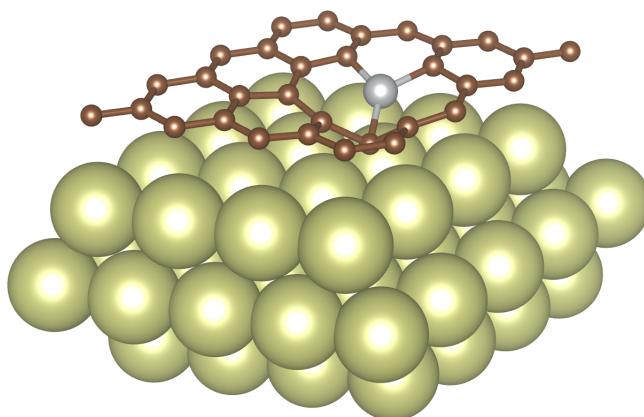
obtained numerically at the reactant, transition and product state, respectively.

Based on our numerically obtained data we can conclude this section's findings by stating that the intercalation of Ni atoms through defect sites in the graphene sheet is a very plausible mechanism to occur at typical annealing temperatures. Additionally, our numerics show that, if the graphene sheet does not feature any vacancy, a large energy barrier prevents any significant contribution to diffusion.

a) Reactant state



b) Transition state



c) Product state

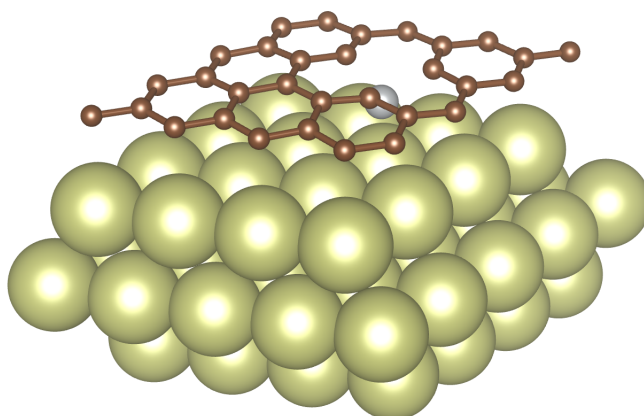


Figure 4.8: Structures from the diffusion process of a single nickel atom through a defective graphene sheet supported by three layers of Ir(111). Shown are the reactant state (**a**), the transition state (**b**) and the product state (**c**), respectively.

4.2 Graphene/Ag(111)/Re(0001)

4.2.1 Experiment

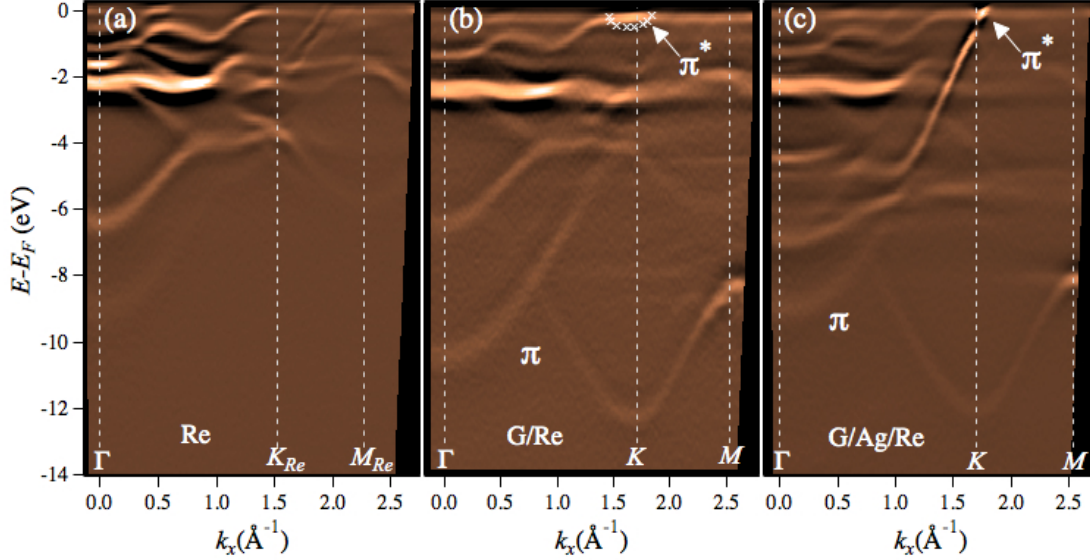


Figure 4.9: Angle-resolved photoemission spectra of (a) a Re surface, (b) Gr/Re and (c) Gr/Ag/Re, respectively. The measurements were conducted by M. Papagno and coworkers [45].

The origin of our numerical investigations were experimental findings by Marco Papagno and coworkers [45], who conducted angle-resolved photoemission experiments to measure the bandstructure of Gr/Ag/Re at 3 different stages of the experimental formation process, starting from a Re substrate as indicated in Fig. 4.9. In a) we see the bandstructure of Re along high-symmetry lines in the first Brillouin zone, from Γ to the K-point and from K to M, respectively. Figure b) was measured after the Re(0001) surface was exposed to ethylene at a temperature of 1100 K. This treatment lead to the formation of a graphene layer on the surface, which is evidenced by the emergence of graphene's π - and σ -bands. The π band now exhibits a parabolic dispersion, as well as a gap of approximately 4 eV at the K-point, which is a sign of a very strong interaction of the graphene sheet with the underlying supporting metal, similar to the behavior of Ni, Ru or Rh, as was mentioned in the introduction of this thesis.

In the final step, Papagno and coworkers deposited two layers of Ag on the Gr sheet, followed by an annealing procedure at 500 K. This process lead to some of the Ag atoms to intercalate and to form a monolayer of Ag between Gr and the Re substrate, whereas the other atoms most presumably desorbed from the surface. Justification for the assumed intercalated monolayer is provided by the bandwidth of the Ag 4d bands, which is smaller than the bandwidth of a Ag multilayer.

The additional intercalated Ag monolayer leads to a reduction of the graphene-substrate interaction and almost recovers graphene’s Dirac cone at the K-point. Although a gap of approx. 450 meV still persists, the linear dispersion in proximity to the Fermi level in k-space re-emerges. Also, corresponding to a charge transfer from the substrate to graphene, a downward shift of the Fermi energy E_F with respect to the Dirac point is observed, enabling the π^* band to be accessible experimentally.

Additional points which we want to analyze more closely are the electronic features at a binding energy of approximately 6 eV, halfway from Γ to K, where the π bands display a band gap. To determine the character of the electronic properties as well as the structure of the present system, we will examine the Gr/Ag/Re system in terms of simple model structures.

4.2.2 Numerics

4.2.2.1 Setup

Within this work spin-polarized DFT calculations have been performed with the *Vienna Ab-initio Simulation Package* (VASP) [24, 22]. We employed PAW potentials [25, 26] and an energy cutoff of 400 eV. To integrate the Brillouin zone a Γ -centered $15 \times 15 \times 1$ k-point mesh was used. All calculations have been carried out in a primitive 1×1 unit cell. In the course of our study, we also employ several choices for exchange-correlation potential approximations, ranging from the local density approximation (LDA) to several incarnations of the generalized gradient approximation (GGA), i.e. PBE [36] and PBE+Grimme [40], as well as the only recently published vdW functional optB88 [38, 39].

4.2.2.2 Lattice constants

As is common practice in the course of a computational analysis, the various lattice constants of the equilibrium structures have to be determined. Since experiment finds Ag to grow pseudomorphically between Gr and Re, we are only left with the identification of the lattice constants of those two materials.

Graphene. As presented in chapter 2, graphene crystallizes in a honeycomb lattice which is described by a Bravais lattice with a two-atom basis. We determine the equilibrium lattice constant by scanning through different lattice constant parameters, which quantity we tune in each numerical run. From the resulting lattice constant a vs. energy plot, the equilibrium constant was obtained by means of finding the minimum of a polynomial interpolating the data set. To be able to compare the behavior of different functionals, we repeat this procedure for LDA, PBE, PBE+Grimme and

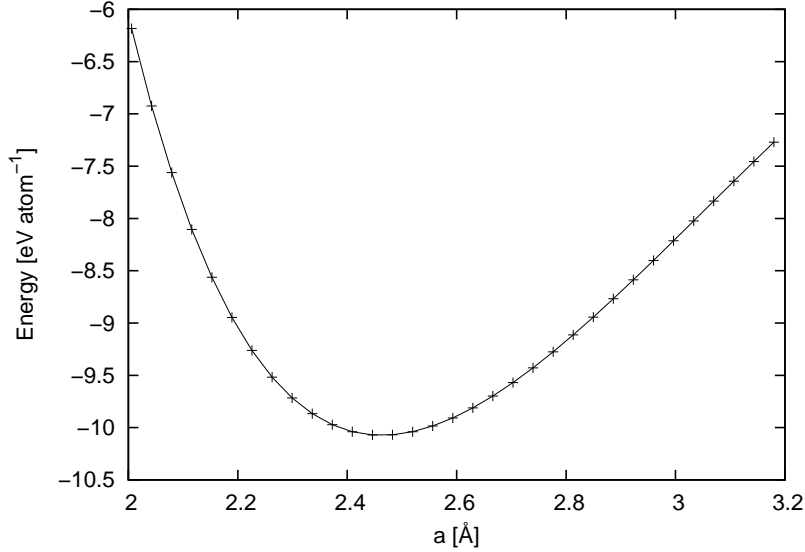


Figure 4.10: Energy [eV] vs. lattice constant [Å], as employed numerically to determine the equilibrium lattice constant a of graphene. In these numerical runs, the optB88 functional was used to approximate the exchange-correlation functional.

optB88. Fig. 4.10 shows the obtained data for the optB88 functional, Tab. 4.1 tabulates the respective data for all the functionals employed as well as the value of a as determined by experiment.

Experimental data suggests an equilibrium lattice constant of 2.46 Å, a value which our numerics reproduce quite well, regardless of the employed functional. In the local density approximation (LDA) the binding is known to be overestimated, in agreement with our data where LDA is the only functional resulting in a lattice parameter *smaller* than experiment, namely 0.54% less. The overbinding can also be easily observed in the equilibrium energy, E_{\min} . Even though the Perdew-Burke-Ernzerhof (PBE) functional performs, as will be shown below, poorly in systems where van-der-Waals (vdW) interaction is of importance, we find the numerically obtained lattice parameter a deviating only by 0.32% from experiment. This agreement can be explained by noting that vdW interaction plays a negligible role in planar graphene, where bonding is

Functional	a [Å]	$\Delta a/a_{\text{exp}}$ [%]	E_{\min} [eV atom ⁻¹]
Experiment	2.46	-	-
LDA	2.44671	-0.540	-10.10005
PBE	2.46777	0.316	-9.22863
PBE+Grimme	2.46765	0.311	-9.28360
optB88	2.46320	0.130	-10.07345

Table 4.1: Experimentally and numerically obtained equilibrium lattice constants a and energies per carbon atom of graphene, calculated for different exchange-correlation potential approximations.

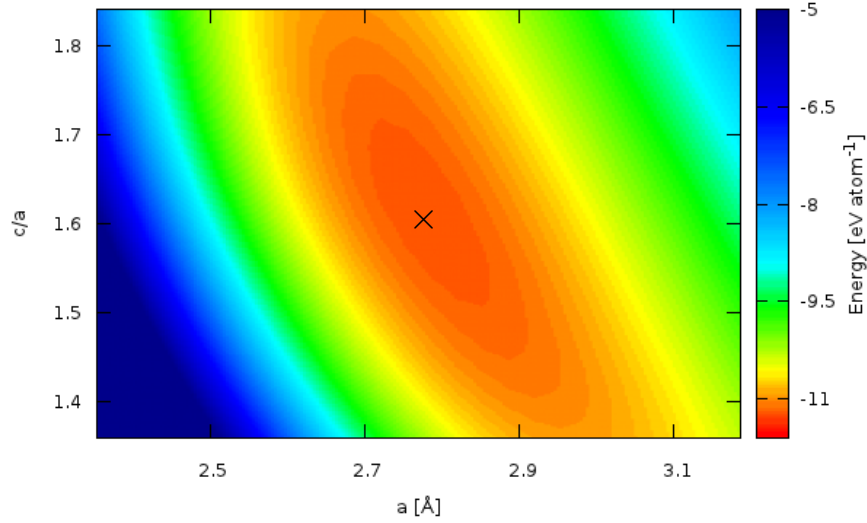


Figure 4.11: Map of the energy [eV] vs. lattice constants a [Å] and c/a , as employed to determine the equilibrium lattice constants a and c/a of Re. Darker colors correspond to a and c/a combinations which are lower in energy. In these runs, the optB88 functional was used as the exchange-correlation functional. \times indicates the minimum energy configuration.

dominated by the strong covalent in-plane σ -bonds. As a result, also PBE's further developed version, PBE+Grimme, which represents an attempt to account for the vdW interaction by means of semi-empirical force field corrections, does not lead to significant enhancements over the PBE data. The lattice parameter a closest to experiment is obtained by means of the vdW functional optB88, which includes a nonlocal energy contribution to approximate nonlocal density correlation effects, differing only by 0.13% from 2.46 Å.

Bulk rhenium. Rhenium's crystal structure is the hexagonal close packed (hcp) lattice, which structure makes it necessary to determine two lattice constants, a and c respectively. In analogy to the energy versus lattice constant scan which we conducted for graphene, we now vary both lattice parameters independently and subsequently extract the equilibrium lattice constants from the minimum of an interpolating function in the three dimensional a vs. c/a vs. energy space (see Fig. 4.11). The respective results are summarized and compared to experiment in Tab. 4.2.

Employing the functionals LDA, PBE, PBE+Grimme and optB88, we see that the in-plane lattice constant a is subject to deviations from the experimental value of 2.761 ranging from -1.73% to 0.59%. As explained above, LDA overestimates the binding, leading to smaller lattice constants and higher binding energies. The out-of-plane lattice parameter c , or, as used computationally, the reduced out-of-plane lattice

Functional	a [Å]	$\Delta a/a_{\text{exp}}$ [%]	c/a	$\Delta(c/a)/(c/a)_{\text{exp}}$ [%]	E_{min} [eV atom ⁻¹]
Experiment	2.761	-	1.61463	-	-
LDA	2.74109	-0.721	1.61387	-0.047	-13.76032
PBE	2.77305	0.436	1.61724	0.161	-12.42284
PBE+Grimme	2.71330	-1.728	1.61237	-0.140	-14.68282
optB88	2.77728	0.590	1.61375	-0.055	-11.27007

Table 4.2: Experimentally and numerically obtained lattice constants a and c/a and equilibrium energies per Re atom, calculated for different exchange-correlation potential approximations.

parameter c/a , features a more uniform behavior throughout the various exchange-correlation functionals. Here the bandwidth of different values only reaches from -0.055% to 0.161%.

Comparison rhenium vs. graphene lattice constant. Tab. 4.3 compares the various deviations of the lattice constants of graphene with the lattice constants of Re and vice versa. Most importantly, we find that the lattice parameter of graphene is about 11% smaller than the one of Re, regardless of the employed functional. This lattice mismatch leaves us with two options for a simplified epitaxial 1×1 model cell, which are to either

1. *stretch the graphene sheet* so that it assumes the structure of the supporting Ag/Re slab, or
2. *compress the substrate* in order to achieve a matching lattice with the terminating graphene layer.

In the present thesis, both options are considered, although we want to stress the fact that, in reality, we would encounter a moiré superstructure which would lie in between those two extremes. This would require a 9×9 graphene cell on an 8×8 Ag/Re cell, as considered in Ref. [45]. This large cell, however, comprises a crucial obstacle. The quantity we are interested in is the system's bandstructure,

Functional	a_{Re} [Å]	a_{Gr} [Å]	$(a_{\text{Re}} - a_{\text{Gr}})/a_{\text{Gr}}$ [%]	$(a_{\text{Gr}} - a_{\text{Re}})/a_{\text{Re}}$ [%]
Experiment	2.761	2.46	12.236	-10.902
LDA	2.74109	2.44671	12.032	-10.740
PBE	2.77305	2.46777	12.371	-11.009
PBE+Grimme	2.71330	2.46765	9.955	-9.054
optB88	2.77728	2.46320	12.751	-11.309

Table 4.3: Comparison of the equilibrium lattice constants of rhenium and graphene, respectively.

which we want to compare to the experimental ARPES data. Yet, the evaluation of the bandstructure is made difficult in this large cell since for the present system an unfolding procedure shows too little significance in the bandstructure plots to be able to make any meaningful assertions [49]. In the following we will thus concentrate on a primitive (1x1) cell which allows a much more simplified discussion of the system's bandstructure.

4.2.2.3 Unit cell preparation

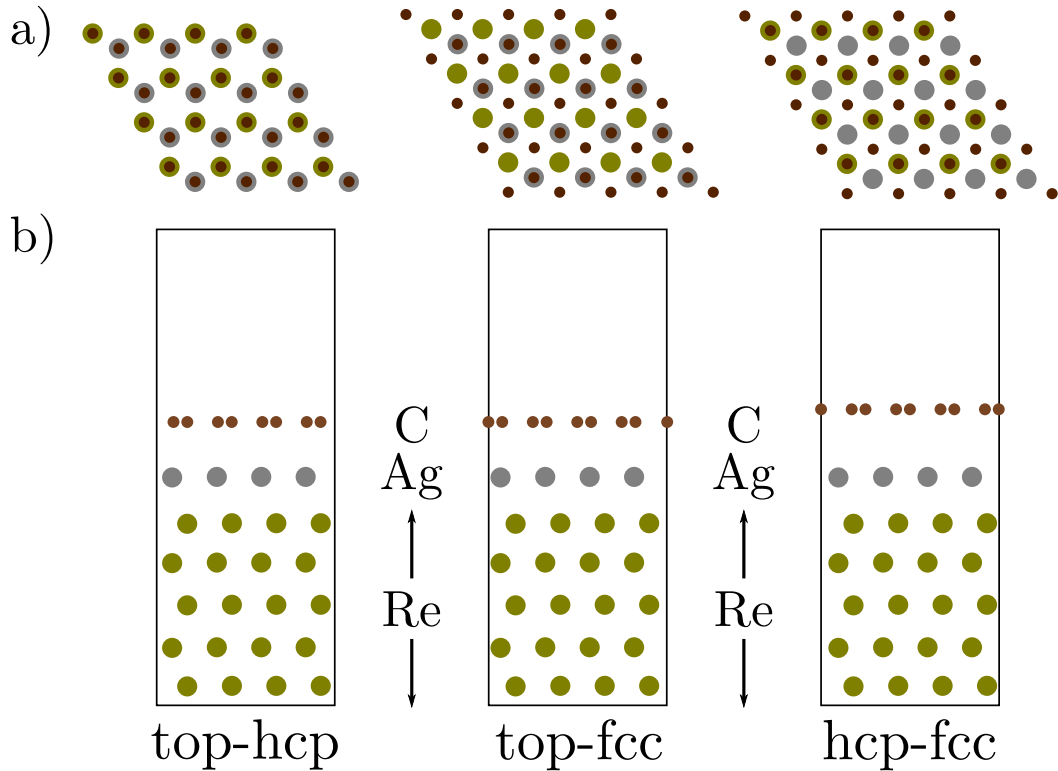


Figure 4.12: Three different interface structures were considered in our numerical treatment of Gr/Ag/Re, namely top-hcp, top-fcc and hcp-fcc. a) and b) show the Gr/Ag/Re cell in a top and side view, respectively. The structural data stems from an actual simulation of graphene on a Ag/Re substrate employing the optB88 functional and was expanded from the 1x1 to a 4x4 cell to achieve better visibility.

To relax the Re slab we fixed the middle layer while the atoms of the adjacent Re bilayers were allowed to move in all directions until all forces were <0.01 eV/Å. The same relaxation procedure was employed following the addition of an Ag monolayer, however restricting the Ag atom's degrees of freedom to the z-coordinate and assuming a continuation of rhenium's hexagonal structure. This resulted in a Ag-substrate distance of 2.5 Å. The bonding distance of the terminating graphene layer was obtained by scanning through different graphene-substrate spacings while allowing an in-plane

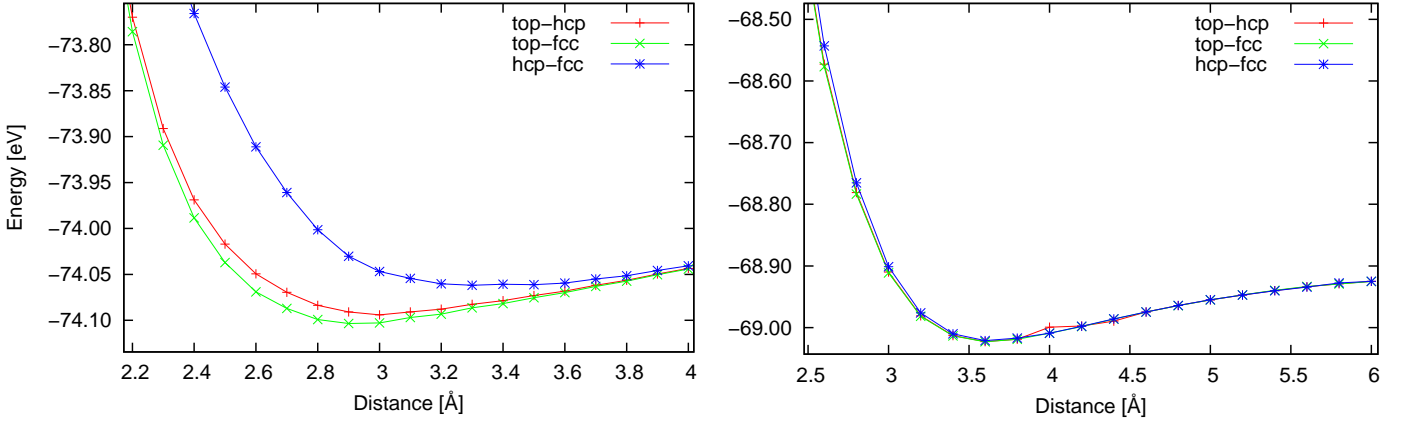


Figure 4.13: Energy [eV] per Gr/Ag/Re unit cell versus graphene-substrate distance d [Å], calculated by means of the optB88 functional for the two models employing the Re (left) and Gr (right) lattice constant and different interface geometries, respectively.

relaxation for both carbon atoms at each numerical run. The placement of graphene's C atoms relative to the substrate was tested with different structures, namely top-hcp, top-fcc and hcp-fcc, respectively. The various adsorption sites are displayed in Fig. 4.12. To the left, we have the two carbon atoms of the unit cell above the metal atoms of the first and second layer, termed the top-hcp arrangement. The figure in the middle corresponds to the top-fcc structure, for which the carbon atoms lie above the top and fcc-hollow site, respectively. In the hcp-fcc interface geometry, the graphene layer is placed such that both the hcp- and fcc-hollow sites are covered if viewed from the top. We want to stress the fact that this list of adsorption sites is not exhaustive and that there exist other interface arrangements, as, e.g., analyzed for Gr/Ni(111) in Ref. [50].

To determine the equilibrium distance between the terminating graphene sheet and the Ag/Re substrate, we scanned through different distances and recorded the energy at each numerical run, for each model and for every adsorption site. Fig. 4.13 shows the obtained energy vs. distance curves for the optB88 functional.

Tab. 4.4 displays a summary of the obtained data. If considering the structure in models based on rhenium's lattice constant (left column of Tab. 4.4), we find that, regardless of the employed functional, the top-fcc adsorption site is determined to be the most stable configuration, featuring the highest binding energy. LDA leads to distances of approximately 2.6 Å, whereas PBE+Grimme and optB88 find a by 0.3 Å larger distance. The PBE functional nearly misses the bonding of the graphene sheet to the substrate with a distance of 4.7 Å. As was already mentioned earlier, this behavior originates in the missing van-der-Waals interaction and demonstrates that this particular choice of functional is inappropriate for the considered system.

The model with $a = a_{Gr}$ exhibits much larger distances compared to the a_{Re}

Functional	Structure	d [\AA]	Functional	Structure	d [\AA]
LDA	top-hcp	2.589	LDA	top-hcp	3.570
	top-fcc	2.573		top-fcc	3.564
	hcp-fcc	3.177		hcp-fcc	3.593
PBE	top-hcp	4.706	PBE	top-hcp	4.654
	top-fcc	4.685		top-fcc	4.400
	hcp-fcc	4.769		hcp-fcc	3.624
PBE+Grimme	top-hcp	2.950	PBE+Grimme	top-hcp	3.269
	top-fcc	2.913		top-fcc	3.266
	hcp-fcc	3.000		hcp-fcc	3.238
optB88	top-hcp	3.000	optB88	top-hcp	3.600
	top-fcc	2.939		top-fcc	3.623
	hcp-fcc	3.300		hcp-fcc	3.624

Table 4.4: Equilibrium graphene-substrate distances d in \AA , tabulated for different functionals and interface structures. The left column corresponds to the toy model employing the lattice constant of rhenium ($a = a_{Re}$), the right column to the lattice parameter of graphene ($a = a_{Gr}$), respectively.

model. Strikingly, there is close to no difference anymore between the different interface structures and, in particular, no distinguished energetically favored adsorption site can be detected throughout the various functionals.

We will now, for the subsequent discussion, only focus on the top-fcc arrangement and optB88, which functional was determined to suit the experimental data best. The final unit cell at a_{Re} features a vacuum distance of 13.2 \AA between consecutive slabs. Since this portion of vacuum might seem too little, we also conducted additional calculations which involved a larger value of 20.0 \AA and as well accounted for dipole corrections by setting the VASP flags `LDIPOL=.TRUE.` and `IDIPOL=3`. The results showed that the energies are sufficiently converged, thus demonstrating that the originally employed vacuum of 13.2 \AA was already enough.

4.2.2.4 Bandstructure

Having now obtained the equilibrium structures for both models, we can evaluate the bandstructures. Fig. 4.14 displays the bandstructures of both models of Gr/Ag/Re, i.e. the models employing the Re and Gr lattice constants, respectively.

Green indicates graphene's π states and red corresponds to the 4d bands of Ag, respectively. The size of the circles indicates the degree of the state's localization and provides information about the character of the different bands. Here we have quite distinct differences between the two bandstructures, but first we want to recapitulate the experimental findings: Ref. [45] found that the intercalated Gr/Ag/Re system features a slight n-doping of graphene, a gap at the K-point and also features a gap of

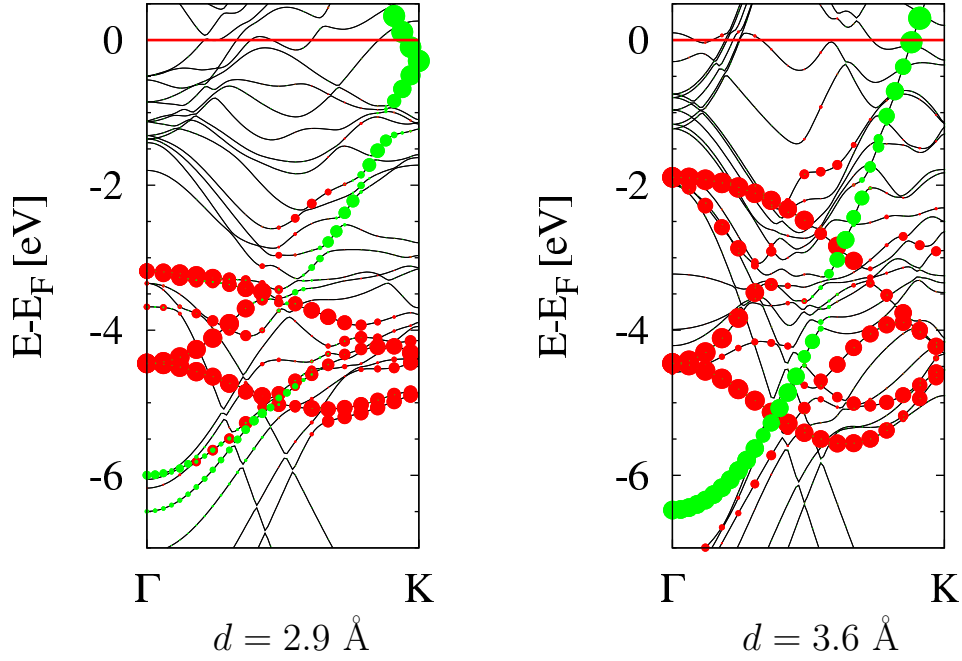


Figure 4.14: Bandstructure of Gr/Ag/Re, employing the equilibrium structures of the Re (left column) and the Gr model (right column) for the functional optB88. The radius of the circles corresponds to the degree of the state's localization. Included are graphene's π -bands (green) and the Ag d-bands (red), respectively. For the former, the radius of the circles has been multiplied by a factor of 5.5 to achieve better visibility, for the latter a factor of 2.5 was employed. The energy is shifted such that the Fermi energy E_F represents the reference energy.

the Gr π band in the middle of the Brillouin zone between Γ and K.

Employing the lattice constant model for a_{Re} (left hand side of Fig. 4.14) at a distance of 2.9 Å, all of these three features are also encountered in our numerics. In qualitative agreement, we find a downward shift of the Dirac point with respect to the Fermi level, corresponding to electron charge transfer from the substrate to the graphene sheet. And, even though it cannot be resolved in Fig. 4.14, we even find a small bandgap of about 16 meV. Our numerics also reproduce the experimentally encountered splitting of the π band, where we have evidence of a hybridization of graphene's π band with the Ag d bands which opens a gap of about 1 eV.

Turning to the model with $a = a_{Gr}$ at a distance $d = 3.6$ Å, which corresponds to a compressed structure compared to the former, we have, at first, a broadening of the bandwidths due to the increased overlap of the various orbitals. With this model we find a splitting of the graphene π states as well, however smaller in magnitude and, additionally, the doping is inverted compared to the lattice constant model of Re. Since this finding represents a major deviation from the experimental data, we will, in the following, employ the lattice constant model of Re exclusively.

The qualitative deviations of both models give rise to the question of whether this

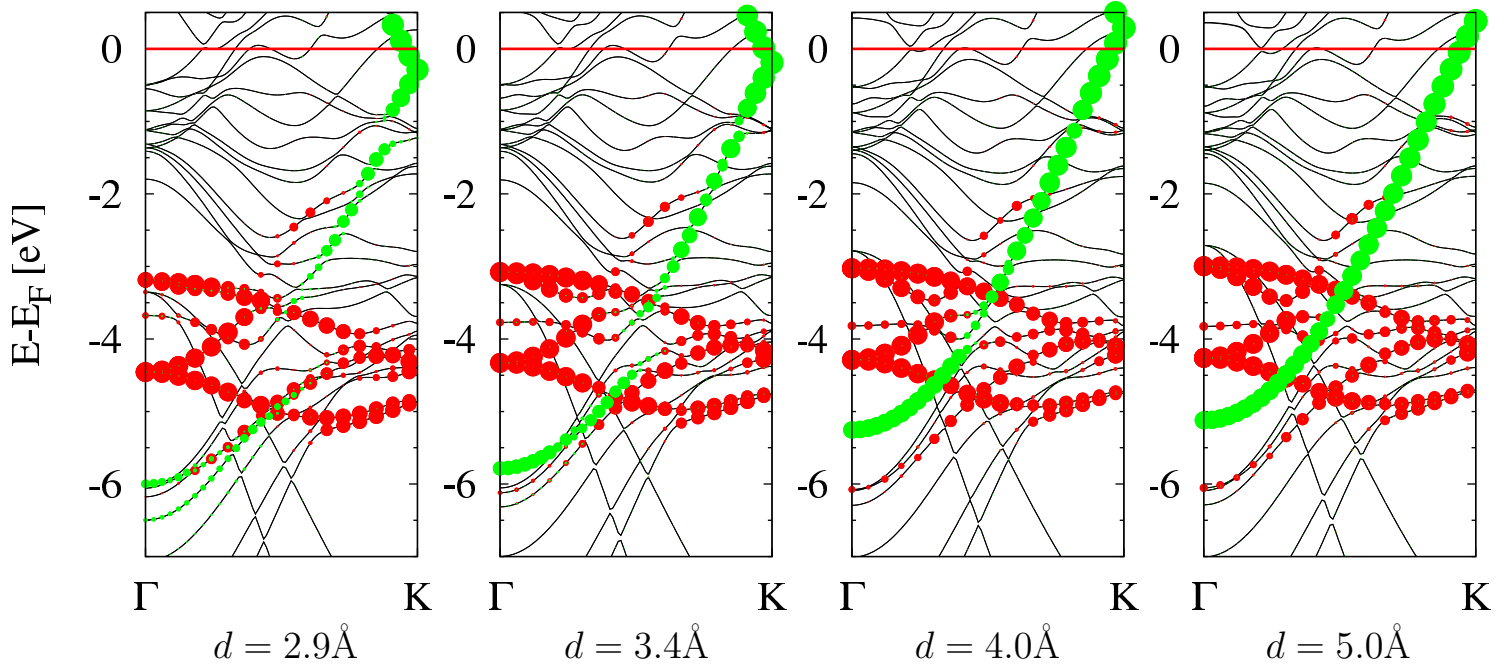


Figure 4.15: Bandstructure of Gr/Ag/Re, employing the optB88 optimized top-fcc structure and equilibrium lattice constant of Re for a selection of different substrate-graphene distances d . The radius of the circles corresponds to the degree of the state's localization. Included are graphene's π -bands (green) and the Ag d-bands (red), respectively. For the former, the radius of the circles has been multiplied by a factor of 5.5 to achieve better visibility, for the latter a factor of 2.5 was employed. The energy is shifted such that the Fermi energy E_F represents the reference energy.

behavior is more controlled by the employed lattice constant, or rather dominated by the different distances d between the graphene sheet and the substrate.

Contribution of distance d . To investigate this assessment, we rerun our calculations for systems in which the distance d was gradually increased from 2.9 Å to 5.0 Å, as shown in Fig. 4.15. Going from the equilibrium distance of 2.9 Å to 5.0 Å, one observes that the splitting of graphene's π -band gets less and less the more the spacing between graphene and Ag/Re is increased. At 5.0 Å, basically no sign of a hybridization is left. We thus have a clear dependence of the hybridization on the distance between graphene and the Ag/Re substrate, since the splitting of the π -band is lost at larger spacings. The numerical data also implies that the larger distance gives rise to a shift of the Dirac point with respect to the Fermi level, where graphene's doping changes from n- to p-doping. Note that we also evaluate the bandstructure close to the equilibrium distance found in a more realistic 9×9 Gr on 8×8 Ag/Re cell, which features a mean spacing of 3.47 Å [45].

To further investigate the (1x1) cell at a distance of 3.4 Å, we now include a

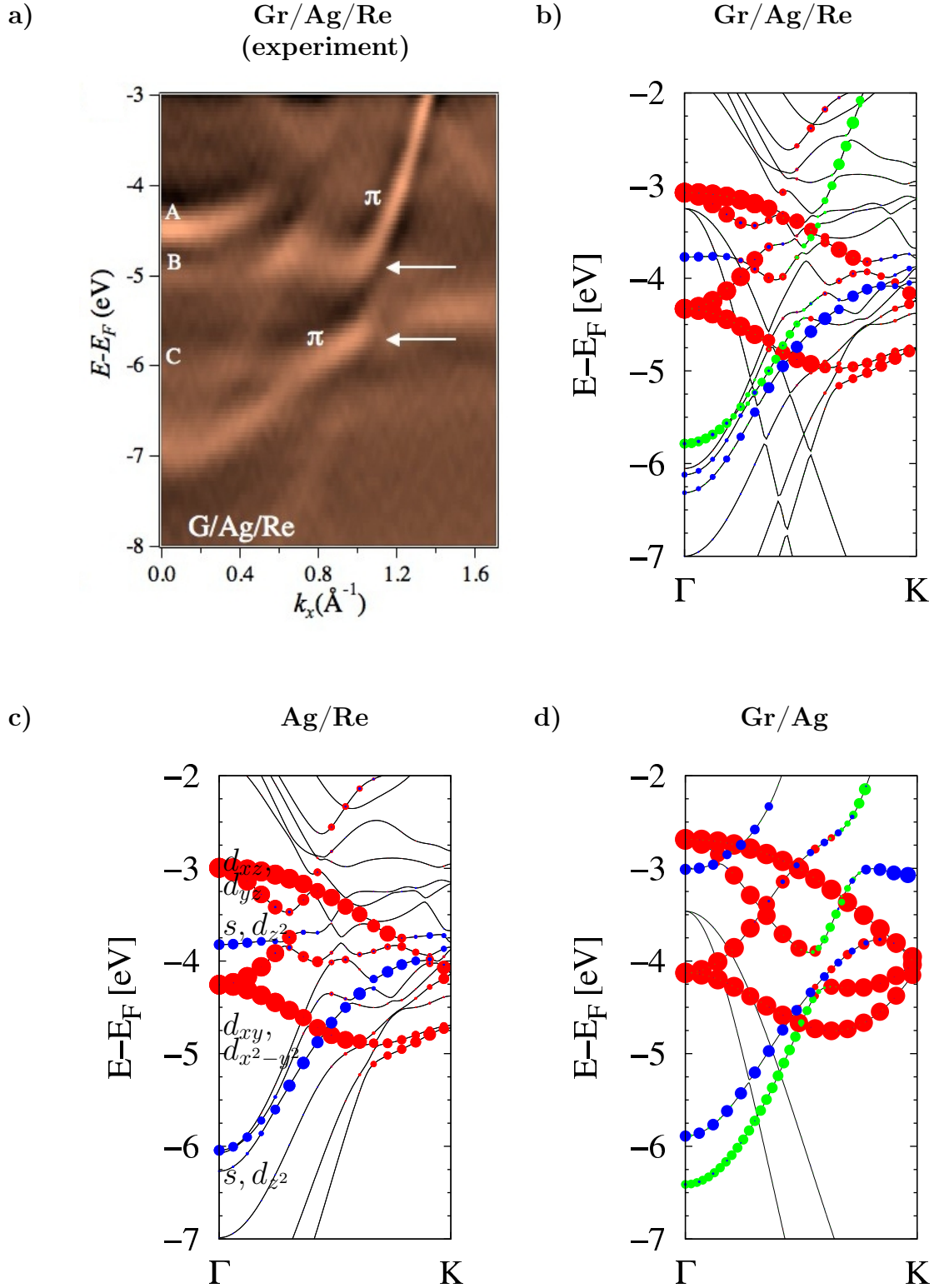


Figure 4.16: Bandstructure of Gr/Ag/Re from experiment [45] (a), of Gr/Ag/Re at a graphene-substrate distance of 3.4 Å (b), of Ag/Re (c) and Gr/Ag (d). The radius of the circles corresponds to the degree of the state's localization. Graphene's π -bands are colored green, silver's s - and d_{z^2} -bands blue and the remaining d -bands are colored red. The energy is shifted such that the Fermi energy E_F represents the reference energy.

close-up of the experimental and DFT bandstructures in Fig. 4.16. Additionally, the bandstructure of Ag/Re and Gr/Ag is shown, i.e. systems where either Gr or the Re substrate have been removed, respectively. Note the extended color code, which now distinguishes between the s, d_{z^2} bands and the $d_{xy}, d_{x^2-y^2}, d_{xz}$ and d_{yz} bands of Ag, respectively. On the left hand side of Fig. 4.16 in (a), we see the electronic features arising from the intercalation, labeled A, B and C, respectively. From the bandstructure of Ag/Re (Fig. 4.16 (c)), one recognizes at the Γ -point two degenerate d_{xz} and d_{yz} states at a binding energy of -3.0 eV, a s, d_{z^2} hybrid state at -3.8 eV, two degenerate d_{xy} and $d_{x^2-y^2}$ states at -4.3 eV and, finally, another s, d_{z^2} hybrid at -6.0 eV below the Fermi energy E_F . With the help of these findings, we can compare the experiment to the full Gr/Ag/Re cell (Fig. 4.16 (b)). Based on these simulations, we assign feature A to the d_{xz}, d_{yz} , B to the s, d_{z^2} and C to the $d_{x,y}, d_{x^2-y^2}$ bands, respectively. Note that the theoretical predictions of the band's position are *higher* in energy. Techniques such as GW which are going beyond standard-DFT to incorporate many-body effects are, however, found to shift the bands to lower values, in almost quantitative agreement with experiment [45].

Graphene adsorbed on a Ag monolayer further illustrates the origin of the bandgap (Fig. 4.16 (d)). On the upper edge, the Gr π -band hybridizes with the s, d_{z^2} bands of Ag whereas on the lower edge a gap is induced by the Ag d_{yz} states. If compared to the results from Gr/Ag/Re, one sees that the Ag d_{yz} states are also subject to a strong hybridization with the Re states, leading to the formation of only a single gap in graphene's π band.

We wish to add that the bandgap's size in the Gr/Ag/Re (1x1) model at a_{Re} might also be underestimated here, since the supercell would allow for graphene's bondlength to be closer to its pristine value which would increasing the bandwidth of the π -band.

Role of Ag monolayer. Finally, to investigate the role of the intercalated monolayer of silver, we run two more calculations. On the one hand, we account for the view that the Ag layer just leads to an increased graphene-substrate distance by completely removing it from our system. This leaves a spacing of 5.4 Å between the Re substrate and the graphene sheet. In the next step, to see the interaction of graphene with Re at closer distance of 2.9 Å, we also evaluate the bandstructure in a system where the Ag layer is chemically interchanged with Re. See Fig. 4.17 for an illustration of these structures.

In the system where the silver monolayer is made invisible, graphene's π - bands show no signs of hybridization, thus displaying bands resembling the ones of ideal graphene, apart from a slight p-doping (see Fig. 4.18). If the Ag layer is replaced by Re, we have signs of a strong interaction of graphene with the Re substrate, show-

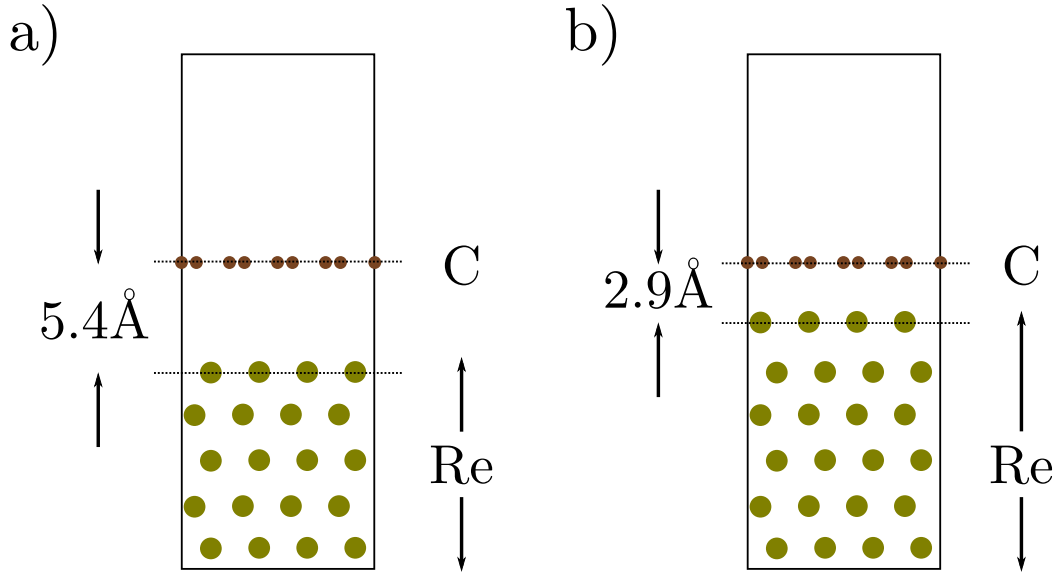


Figure 4.17: Cell configuration of graphene supported by five (six) layers of rhenium, featuring a graphene-substrate distance of 5.4 Å (2.9 Å). The structure was expanded from the 1x1 to a 4x4 cell to achieve better visibility.

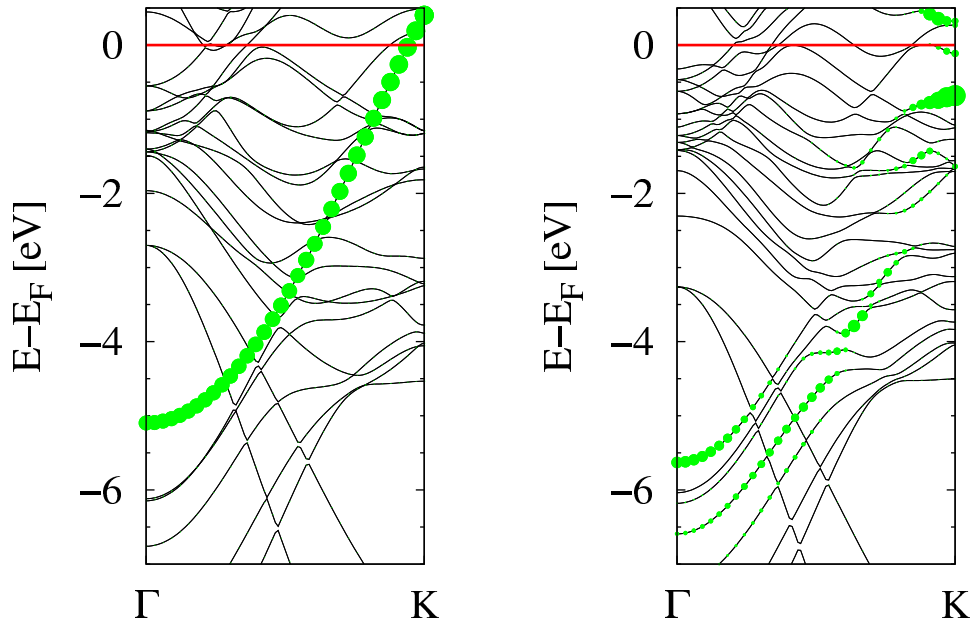


Figure 4.18: Bandstructure of graphene supported by five (six) layers of rhenium, featuring a graphene-substrate distance of 5.4 Å (2.9 Å). The radius of the circles corresponds to the degree of the state's localization. Graphene's π -bands are colored green. The different geometries correspond to the structures depicted in Fig. 4.17. The energy is shifted such that the Fermi energy E_F represents the reference energy.

ing numerous bandgaps which lead to a disruption of graphene's π band. The band splitting, however, takes place in different parts of the Brillouin zone, as opposed to the behavior predicted by experiment. We can, therefore, clearly conclude that the experimentally observed splitting is entirely due to a hybridization of the π -band of graphene with the d-bands of silver.

Chapter 5

Summary and Outlook

By way of numerical ab-initio simulations employing the *Vienna Ab-initio Simulation Package* VASP we analyzed the properties of intercalated systems featuring a terminating graphene layer on top of a supporting substrate. Motivated by experimental data put forward by M. Fonin et al. in Ref. [44] and M. Papagno and coworkers in Ref. [45], we investigated intercalation processes of Ni under Gr/Ir(111) and the electronic structure of Gr/Ag/Re(0001).

We could demonstrate that the diffusion of a single Ni atom through a pristine, ideal graphene sheet faces an energy barrier of almost 12 eV, thus revealing that this process is of no significance in experiment. This assessment, however, is only applicable to graphene sheets which feature no defects. As soon as a single vacancy is introduced into the honeycomb lattice the corresponding barrier is lowered by approximately 10 eV. In the full system where we allowed for an Ir(111) support of the defective graphene layer, this quantity is even reduced further to 1.5 eV, rendering this process a very likely one to occur at experimentally employed annealing temperatures.

Since our results hint at an extremely weak contribution from intercalation at intact lattice sites, we didn't examine reaction processes for supported systems with a pristine graphene sheet. The question of whether other reaction mechanisms are responsible for larger reaction rates, as e.g. speculated in Ref. [44], remains. Huang et al. [51], for instance, assessed the diffusion through a pristine graphene sheet under the assumption of a defect-creation and subsequent self-healing process of the C-C bonds. The assessment of such mechanisms, however, is made difficult since the method we employ requires an already good guess of the reaction mechanism. The evaluation of these mechanisms is therefore left for future investigations.

The second part of this thesis is related to the structural and electronic properties of Gr/Ag/Re, for which ARPES data suggests a weaker-than-expected decoupling of graphene from the Re substrate after the intercalation of a monolayer of Ag. This is in contrast to the currently common view, where incorporated layers of less reactive noble

metal atoms are thought of as a spacer which reduces the orbital's overlap and, thus, the interaction. To reveal the nature of this finding, we study Gr/Ag/Re in a simplified (1x1) cell approach employing two limiting models featuring the lattice constants of either Re or Gr, respectively. Our data agree with photoemission experiments, showing that the residual interaction stems from a hybridization of graphene's π -states with the d-states of Ag, inducing a bandgap in the π -band. Hence, we can state that the electronic structure of graphene adsorbed on a noble metal/metal interface may still deviate significantly from the behavior of an ideal, unsupported graphene sheet.

Appendix

In the course of this thesis a lot of situations arose where the existing tools for computer based operations proved inadequate and troublesome. These difficulties came into play while working on clusters using the Sun-Grid-Engine (SGE) or while trying to visualize VASP data with the need for special requirements. A lot of work went into the development of these scripts and it is thus the author's wish to share them in order to spare future users the task of writing similar tools themselves.

1 SGE job script

`subSGE.sh` was written to simplify the work with the SGE queuing system. While having the program VASP in mind, the script can run any executable as specified by the `-p` option or by setting the `PROGRAM` variable manually in the source file.

```
1
2
3  #!/ bin / bash
4
5  ##
6  ##  subSGE.sh
7  ##
8  # submit job using the Sun-Grid-Engine queuing system
9  #
10
11  ### FUNCTIONS ###
12  function printUsage() {
13      cat <<-EOF
14          usage: $0
15              [ -e "script" ... execute bash script ]
16              [ -s "NSLOTS" ... use NSLOTS nodes ]
17              [ -h ... execute VASP in current directory ]
18              [ -p "executable" ... execute program different from VASP ]
19              [ -g ... use gamma-only vasp version ]
20  EOF
```

```

21 }
22
23 ### PARSE INPUT ###
24 PROGRAM="vasp"    # enter executable name here
25
26 while getopts e:s:hgp: OPTS
27 do
28     case $OPTS in
29         e) EXEC=$OPTARG;;
30         s) NNODES=$OPTARG;;
31         g) PROGRAM="vasp_gamma";;
32         p) PROGRAM=$OPTARG;;
33         h)
34             RUN="run.sh"
35             cat > $RUN <<-EOF
36                 mpirun -machinefile \${TMPDIR}/machines -envall -np \${NSLOTS}
37                     $PROGRAM
38             EOF
39             EXEC=$RUN
40             ;;
41         esac
42     done
43
44 ### VARIABLE CHECK ###
45 if [[ -z $EXEC ]]; then
46     # if no executable shell script is specified, search for *.sh in
47     # current directory; exit if more than one or no *.sh is found
48     SH_SCR=$(ls | grep ".sh")
49     SH_NUM=$(echo "$SH_SCR" | wc -l)
50     if [[ "$SH_NUM" -eq "1" ]]; then
51         EXEC="$SH_SCR"
52     else
53         printUsage
54         exit 1
55     fi
56 fi
57
58 if [[ -z $NNODES ]]; then
59     # set NNODES=16 if no arguments are supplied
60     NNODES="16"
61 fi
62
63 ### WRITE/SUBMIT SGE_JOBSCRIPT ###
64 SGE_JOBNAME=$(echo $EXEC | sed 's/.sh//g')
65 SGE_JOBSCRIPT="SGE_JOBSCRIPT.sh"

```

```

66 cat > $SGE_JOBSCRIPT <<-EOF
67     #!/ bin / bash
68
69     ### SGE Parameters ###
70     #$ -N ${SGE_JOBNAME}
71     #$ -o "temp_${SGE_JOBNAME}.dat"
72     #$ -q all.q
73     #$ -j y
74     #$ -pe mpich $NNODES
75     #$ -S / bin / bash
76     #$ -cwd
77     #$ -V
78     source \ $SGE_O_WORKDIR / $EXEC
79     exit
80 EOF
81
82 qsub $SGE_JOBSCRIPT
83
84 ### CLEANUP ###
85 rm $SGE_JOBSCRIPT
86 if [[ ! -z $RUN ]]; then
87     rm $RUN
88 fi

```

2 Visualize ionic relaxation

During the evaluation of the diffusion data from the first part of chapter 4 it became painfully evident that existing tools like p4vasp don't offer a way to visualize the system's configuration for each relaxation step, let alone the forces acting on the various ions. The following set of scripts was thus written as a package to control the numerical runs underlying the dimer method calculations, but they can also be used for monitoring any relaxation procedure from VASP output. The program which was found to perfectly suit this kind of requirements is `xmakemol`¹, which reads in positional data in .xyz format and additionally allows for the display of vectors at each ion to visualize the acting forces.

The following script `xmake.sh` is meant to be executed in the same directory as the VASP run. The correct usage is included in the source file. `visualizeRelaxation.sh` extracts the number of ionic steps from the OUTCAR, the ionic coordinates from the XDATCAR and the forces acting on each ion at each numerical step from the OUTCAR file of VASP. `xmakemol` is then able to separately display every ionic step and can

¹www.nongnu.org/xmakemol/

even animate the relaxation. Note that `visualizeRelaxation.sh` also distinguishes between atomic species, i.e. different ions are colored differently if the output is read in by `xmakemol`.

The script `showUnstableModes.sh` was written to facilitate the evaluation of unstable modes from the vibrational spectrum analysis required for the dimer method. It searches the file `OUTCAR` for entries with imaginary frequency and outputs the cell configuration including the mode's directions in `.xyz` format.

2.1 xmake.sh

```

1
2
3  #!/ bin / bash
4
5  ####
6  #### xmake.sh
7  ####
8  # view/animate VASP data in xmakemol from an existing .xyz file
9  # or a file generated by visualizeRelaxation.sh and/or
10 # showUnstableModes.sh
11 #
12
13 #
14 # usage: $0
15 # [ -f ... execute "visualizeRelaxation.sh > tmp; xmakemol -f tmp" ]
16 # [ -d ... execute "showUnstableModes.sh > tmp; xmakemol -f tmp" ]
17 # [ -i "input" ... open input file given in .xyz format)]
18 #
19
20 #### INPUT ####
21 INPUT="$2"
22
23 #### PARSE INPUT ####
24 while getopts i:fd OPTS
25 do
26     case $OPTS in
27         f)
28             ARGS="visualizeRelaxation.sh > tmp; xmakemol -f tmp";;
29         d)
30             ARGS="showUnstableModes.sh > tmp; xmakemol -f tmp";;
31         i)
32             ARGS="xmakemol -f $INPUT";;
33     esac
34 done

```

```

35
36 ### MAIN ###
37 eval "$ARGS"

```

2.2 visualizeRelaxation.sh

```

1
2
3 #!/bin/bash
4
5 ###
6 ### visualizeRelaxation.sh
7 ###
8 # extract forces and ionic coordinates from OUTCAR, OSZICAR and XDATCAR
9 # and save in .xyz format to view/animate in xmakemol
10 #
11
12 ### get # of ionic steps from OSZICAR ###
13 NSTEPS=$(cat OSZICAR | grep 'F=' | tail -1 | awk '{print $1}')
14 ### get # of ions ###
15 NIONS=$(cat XDATCAR | \
16     awk 'NR==7 { sum=0
17         for ( j=1;j<=NF;j=j+1 ) sum=sum+$j
18         print sum }'
19     )
20 ### scaling factor of forces ###
21 SCALE=1
22
23 for (( i=0;i<=$((NSTEPS-1));i++ )); do
24 #for (( i=$((NSTEPS-1));i>=0;i-- )); do    <--- USE TO VIEW RELAXATION IN
    REVERSED ORDER
25     cat OUTCAR | grep TOTAL-FORCE -A$((NIONS+1)) | sed '/--/d' | \
26     awk -v i=$i -v NIONS_TOT=$NIONS -v SCALE=$SCALE '
27     BEGIN {
28         LC=0
29         while( getline < "XDATCAR" > 0 )
30         {
31             if( LC == 6 ) {
32                 for ( j=1;j<=NF;j=j+1 ) {
33                     NSPECIES=NF; NIONS[j]=$j
34                     NIONS_TOT=0; for ( k=1;k<=NF;k++ ) NIONS_TOT=NIONS_TOT+$k
35                 }
36             }
37             LC++
38             if( LC == 6 ) {for ( j=1;j<=NF;j++ ) {IONS[j]=$j}}

```

```

39     }
40     print NIONS_TOT
41     print "FORCE:" " Scaling factor:" SCALE " Iteration:" i+1
42 }
43 {
44     FLAG="UNSET"
45     if ( NR>=i*(NIONS_TOT+1)+2 && NR<=(i+1)*(NIONS_TOT+1) )
46     {
47         for ( j=1;j<=NSPECIES;j++)
48         {
49             NIONS_CURR=0
50             for ( k=1;k<=j ;k++)
51             {
52                 NIONS_CURR=NIONS_CURR+NIONS[k]
53             }
54             if ( (NR-i*(NIONS_TOT+1))<=1+NIONS_CURR && FLAG=="UNSET")
55             {
56                 ION=IONS[j]; FLAG="SET"
57             }
58         }
59         printf "%-5s %9.6f %9.6f %9.6f \t %-15s %9.6f %9.6f %9.6f \n",
60             ION,$1,$2,$3,"atom_vector",SCALE*$4,SCALE*$5,SCALE*$6
61     }
62 }',
63 done

```

2.3 showUnstableModes.sh

```

1
2
3  #!/bin/bash
4
5  ###
6  ### showUnstableModes.sh
7  ###
8  # extract displacement directions and ionic
9  # coordinates from OUTCAR, OSZICAR and XDATCAR
10 # after a vibrational modes calculation and save in .xyz
11 # format to view in xmakemol
12 #
13
14 ### get # of ionic steps from OSZICAR ###
15 NSTEPS=$(cat OUTCAR | grep f/i | wc -l)
16 ### get # of ions ###
17 NIONS=$(cat XDATCAR | \

```

```

18     awk 'NR==7 { sum=0
19         for ( j=1;j<=NF;j=j+1 ) sum=sum+$j
20         print sum }'
21     )
22     ### scaling factor of forces ###
23     SCALE=40
24
25     for (( i=0;i<=$((NSTEPS-1));i++)); do
26         cat OUTCAR | grep f/i -A$((NIONS+1)) | sed '/--/d' | sed '/dx/d' |
27         sed 's/-/ -/g' | \
28         awk -v i=$i -v NIONS=$NIONS -v SCALE=$SCALE '
29         BEGIN {
30             print NIONS
31             print "FORCE:"
32         }
33         NR>1+i*(NIONS+1)&&NR<1+(i+1)*(NIONS+1) {
34             if ( NR == (i+1)*(NIONS+1) ) ION="Ni"; else ION="C"
35             printf "%-5s %9.6f %9.6f %9.6f \t %-15s %9.6f %9.6f %9.6f \n",
36                 ION,$1,$2,$3,"atom_vector",SCALE*$4,SCALE*$5,SCALE*$6
37         }'
38     done

```

3 Reaction coordinate

This script corresponds to the numerical implementation of Eq. (4.1) to obtain the energy diagrams from relaxation runs. Both the OSZICAR and XDATCAR files are needed.

```

1
2
3     #!/bin/bash
4
5     ###
6     ### getReactionCoordinate.sh
7     ###
8     # extract energy vs. reaction coordinate from OSZICAR and XDATCAR
9     #
10
11     ### temporary file ###
12     TMP="TMP1.dat"
13     TMP2="EvsD.dat"
14     ### get # of ionic steps from OSZICAR ###
15     NSTEPS=$((cat OSZICAR | grep 'F=' | tail -1 | awk '{print $1}'))

```



```

16  ### cellheight ###
17  zCELL=$(cat CONTCAR | awk 'NR==2 {a0=$1}; NR==5 {c0=$3}; NR==41 {z0Ni=
    $3}; END {print a0*c0}')
18  ### get # of ionic coordinates ###
19  NIONS=$(cat XDATCAR | awk 'NR==7 {sum=0; for ( j=1;j<=NF;j=j+1 ) sum=
    sum+$j; print sum}')
20  ### # of lines in XDATCAR in front of ionic positions ###
21  NXDATCAR="8"
22
23  for i in $(seq -1 1 $((NSTEPS-1-2))); do
24      zNi=$(cat XDATCAR | awk -v i=$i -v zCELL=$zCELL -v NIONS=$NIONS -v
        NXDATCAR=$NXDATCAR '
25          BEGIN {r=0;s=0;t=0;sum=0;sum_x=0;sum_y=0;sum_z=0}
26          {
27              for ( k=1;k<=3;k++) {
28                  if( NR==2+k ) {
29                      # get bravais matrix
30                      v[k,1]=$1; v[k,2]=$2; v[k,3]=$3
31                  }
32              }
33          }
34          {
35              for ( k=1;k<=NIONS;k++ ) {
36                  if( NR==NXDATCAR+(NIONS+1)*(i)+k ) {
37                      # get old configuration
38                      x_old[k,1]=$1*v[1,1]+$2*v[2,1]+$3*v[3,1]
39                      x_old[k,2]=$1*v[1,2]+$2*v[2,2]+$3*v[3,2]
40                      x_old[k,3]=$1*v[1,3]+$2*v[2,3]+$3*v[3,3]
41                  }
42                  if( NR==NXDATCAR+(NIONS+1)*(i+1)+k ) {
43                      # get new configuration
44                      x_new[k,1]=$1*v[1,1]+$2*v[2,1]+$3*v[3,1]
45                      x_new[k,2]=$1*v[1,2]+$2*v[2,2]+$3*v[3,2]
46                      x_new[k,3]=$1*v[1,3]+$2*v[2,3]+$3*v[3,3]
47                      # RMS change from x_old to x_new
48                      sum_x=sum_x+(x_new[k,1]-x_old[k,1])**2
49                      sum_y=sum_y+(x_new[k,2]-x_old[k,2])**2
50                      sum_z=sum_z+(x_new[k,3]-x_old[k,3])**2
51                      sum=sqrt(sum_x+sum_y+sum_z)
52                  }
53              }
54          }
55      END {
56          if ( i==1 ) {print 0.0} else {print sum}
57      },
58  )

```

```
59 E=$(cat OSZICAR | grep " $((i+1+1)) F" | awk '{print $5}')
60 echo $zNi $E >> $TMP
61 cat $TMP | awk '{ sum+=$1; print sum, $2}' > $TMP2
62 rm $TMP
63 done
```

Acknowledgements

At this place I want to thank my supervisors Prof. Josef Redinger and Dr. Florian Mittendorfer as well as DI Andreas Garhofer for their support during the writing of the present thesis. Further thanks are due to Wernfried Mayr-Schmölzer and Dipl.-Phys. Marcel Hieckel for offering me their expertise and sharing their code, greatly facilitating problems occurring in the practical treatment of this work.

I also want to express my gratitude for the grant provided by project I422-N16 of the Austrian Science Foundation (FWF) as part of the European Science Foundation (ESF) EUROCORES project EuroGRAPHENE/SpinGraph, which, in further consequence, also enabled the collaborations that led to the subjects treated in this thesis.

Finally, I want to thank my parents, family and close friends for providing me with encouragement and confidence in situations where finishing my studies seemed like a hopeless endeavour. All of this wouldn't have been possible without you.

Bibliography

- [1] K. S. Novoselov *et al.*, Science **306**, 666 (2004).
- [2] K. S. Novoselov *et al.*, Proceedings of the National Academy of Sciences of the United States of America **102**, 10451 (2005).
- [3] F. Schwierz, Nat Nano **5**, 487 (2010).
- [4] A. K. Geim and K. S. Novoselov, Nature Materials **6**, 183 (2007).
- [5] A. K. Geim and P. Kim, Scientific American **298**, 90 (2008).
- [6] A. K. Geim and A. H. MacDonald, Physics Today **60**, 35 (2007).
- [7] P. Sutter, J. T. Sadowski, and E. Sutter, Physical Review B **80**, 245411 (2009).
- [8] I. Pletikosić *et al.*, Physical Review Letters **102**, 056808 (2009).
- [9] A. T. N'Diaye, S. Bleikamp, P. J. Feibelman, and T. Michely, Physical Review Letters **97**, 215501 (2006).
- [10] L. Gao, J. R. Guest, and N. P. Guisinger, Nano Letters **10**, 3512 (2010).
- [11] A. L. Walter *et al.*, Physical Review B **84**, 195443 (2011).
- [12] A. Varykhalov *et al.*, Phys. Rev. Lett. **101**, 157601 (2008).
- [13] A. Varykhalov, M. Scholz, T. Kim, and O. Rader, Physical Review B **82**, 121101 (2010).
- [14] C. Enderlein, Y. S. Kim, A. Bostwick, E. Rotenberg, and K. Horn, New Journal of Physics **12**, 033014 (2010).
- [15] P. W. Sutter, J.-I. Flege, and E. A. Sutter, Nature Materials **7**, 406 (2008).
- [16] P. Sutter, M. S. Hybertsen, J. T. Sadowski, and E. Sutter, Nano Letters **9**, 2654 (2009).

-
- [17] P. R. Wallace, Physical Review Online Archive (Prola) **71**, 622 (1947).
 - [18] A. H. C. Neto, F. Guinea, N. M. R. Peres, K. S. Novoselov, and A. K. Geim, Reviews of Modern Physics **81**, 109 (2009), 0709.1163.
 - [19] T. Ihn, *Semiconductor nanostructures: quantum states and electronic transport* (Oxford Univ. Press, 2010).
 - [20] S. Reich, J. Maultzsch, C. Thomsen, and P. Ordejón, Physical Review B **66**, 035412 (2002).
 - [21] M. I. Katsnelson, K. S. Novoselov, and A. K. Geim, Nature Physics **2**, 620 (2006).
 - [22] G. Kresse and J. Hafner, Physical Review B **47**, 558 (1993).
 - [23] G. Kresse and J. Hafner, Phys. Rev. B **49**, 14251 (1994).
 - [24] G. Kresse, Computational Materials Science **6**, 15 (1996).
 - [25] P. E. Blöchl, Physical Review B **50**, 17953 (1994).
 - [26] G. Kresse and D. Joubert, Physical Review B **59**, 1758 (1999).
 - [27] W. A. Harrison, *Electronic structure and the properties of solids: the physics of the chemical bond* (Dover Publications, 1989).
 - [28] R. M. Martin, *Electronic structure: basic theory and practical methods* (Cambridge University Press, 2004).
 - [29] M. Kreuzer, Quantum theory, Lecture Notes, 2007.
 - [30] S. Bühler-Paschen and P. Mohn, Festkörperphysik II, Lecture Notes, 2007.
 - [31] C. Fiolhais, F. Nogueira, and M. Marques, *A primer in density functional theory* (Springer, 2003).
 - [32] M. Born and R. Oppenheimer, Ann. Phys. **389**, 457 (1927).
 - [33] W. Kohn and L. J. Sham, Physical Review Online Archive (Prola) **140**, A1133 (1965).
 - [34] P. Hohenberg and W. Kohn, Physical Review Online Archive (Prola) **136**, B864 (1964).
 - [35] W. Kohn, Reviews of Modern Physics **71**, 1253 (1999).

-
- [36] J. P. Perdew, K. Burke, and M. Ernzerhof, *Physical Review Letters* **77**, 3865 (1996).
- [37] M. Vanin *et al.*, *Physical Review B* **81**, 081408 (2010), 0912.3078.
- [38] J. Klimeš, D. R. Bowler, and A. Michaelides, *Journal of Physics: Condensed Matter* **22**, 022201 (2010).
- [39] J. Klimeš, D. R. Bowler, and A. Michaelides, *Physical Review B* **83**, 195131 (2011).
- [40] S. Grimme, *J. Comput. Chem.* **27**, 1787 (2006).
- [41] W. von der Linden, F. G., and S. B., *Quantenmechanik, Lecture Notes*, 2000.
- [42] U. Zimmerli, M. Parrinello, and P. Koumoutsakos, *The Journal of Chemical Physics* **120**, 2693 (2004).
- [43] M. Dion, H. Rydberg, E. Schröder, D. C. Langreth, and B. I. Lundqvist, *Physical Review Letters* **92**, 246401 (2004).
- [44] M. Sicot *et al.*, *ACS Nano* **6**, 151 (2012).
- [45] M. Papagno *et al.*, Evidence of strong interaction between graphene and a Ag monolayer supported on Re(0001), Unpublished, 2012.
- [46] G. Henkelman and H. Jónsson, *The Journal of Chemical Physics* **111**, 7010 (1999).
- [47] G. Henkelman, G. Jóhannesson, and H. Jónsson, *Methods for Finding Saddle Points and Minimum Energy Paths*, pp. 269–302, 2001.
- [48] A. Heyden, A. T. Bell, and F. J. Keil, *The Journal of Chemical Physics* **123**, 224101 (2005).
- [49] W. Ku, T. Berlijn, and C. C. Lee, *Physical Review Letters* **104**, 216401 (2010).
- [50] M. Fuentes-Cabrera, M. I. Baskes, A. V. Melechko, and M. L. Simpson, *Physical Review B* **77**, 035405 (2008).
- [51] L. Huang *et al.*, *Applied Physics Letters* **99**, 163107 (2011).

List of Figures

2.1	Honeycomb lattice of graphene.	11
2.2	Unit cell of graphene. The two different sublattices are indicated by coloured circles.	12
2.3	Tight-binding bandstructure of graphene's π - and π^* -bands. a) Bands along the closed path $K \rightarrow \Gamma \rightarrow M \rightarrow K$ in the first Brillouin zone. b) Linear dispersion of the valence and conduction bands in proximity to the K-point. The green lines indicate perfectly linear behavior. c) First Brillouin zone of graphene, including points of high symmetry. c) Density of states per unit cell as determined by Eq. (14) in Ref. [18]. .	16
3.1	Flow chart illustrating the procedure to solve Eq. (3.23), as presented in Ref. [31].	24
3.2	Two hydrogen atoms A and B, well separated by a distance $\mathbf{R} \gg \mathbf{r}_A, \mathbf{r}_B$. The coordinate \mathbf{r}_i correspond to the vectors pointing from the protons to the adjacent electrons.	26
4.1	STM image of an intercalated Ni island underneath Gr/Ir(111) as found in experiment. The inset at the bottom sketches the fact that islands can also be found underneath areas of unmodified graphene sheets. This figure was taken from Ref. [44].	30
4.2	Schematic illustration of the experimental annealing process to achieve intercalation. In the first step graphene is grown on the surface. The foreign atoms are then positioned on top of the Gr/metal system, followed by annealing. During the heat exposure intercalation occurs by atoms diffusing through the graphene sheet.	31

4.3	Sketch of the fixed coordinate method, as employed in our numerics. The z-distance of the diffusing atom is decreased gradually. We show here two examples of the fixed coordinate approach in a 4x4 unit cell, i.e. the diffusion through a pristine graphene sheet (left) and through a vacant site in the graphene layer (right), respectively. For simplicity the cell is depicted using a wireframe representation.	32
4.4	a) Structures of the p(4x4) cell at the initial (left) and transition state (right). b) Total energy of the unit cell [eV] as a function of the reaction coordinate [\AA], shifted to feature the initial state as the reference energy. The unit cell consists of 32 carbon atoms and one Ni atom, respectively. For the fixed coordinate model (left panel), black lines are included which correspond to the transition state and the $d = 7.5 \text{ \AA}$ configuration. The right panel displays the barrier as obtained by the dimer method. Note that both approaches use different definitions of the reaction coordinate, the x-coordinates are therefore not to scale (see text for details).	35
4.5	a) Structures of the p(4x4) cell at the initial (left) and transition state (right). b) Total energy of the unit cell [eV] as a function of the reaction coordinate [\AA], shifted to feature the initial state as the reference energy. The unit cell consists of 31 carbon atoms and one Ni atom, respectively. For the fixed coordinate model (left panel), black lines are included which correspond to the transition state and the $d = 7.5 \text{ \AA}$ configuration. The right panel displays the barrier as obtained by the dimer method. Note that both approaches use different definitions of the reaction coordinate, the x-coordinates are therefore not to scale (see text for details).	36
4.6	a) Structures of the p(8x8) cell at the initial (left) and transition state (right). b) Total energy of the unit cell [eV] as a function of the reaction coordinate [\AA], shifted to feature the initial state as the reference energy. The unit cell consists of 127 carbon atoms and one Ni atom, respectively. For the fixed coordinate model (left panel), black lines are included which correspond to the transition state and the $d = 7.5 \text{ \AA}$ configuration. The right panel displays the barrier as obtained by the dimer method. Note that both approaches use different definitions of the reaction coordinate, the x-coordinates are therefore not to scale (see text for details).	37

4.7	Total energy of the unit cell [eV] as a function of the reaction coordinate [\AA] as obtained by the dimer method, shifted to feature the initial state as the reference energy. The unit cell consists of 48 Ir atoms, 31 carbon atoms and one Ni atom. Black lines are included which correspond to the initial state (at 0.0 eV), transition state (at 1.50 eV) and the final state (-1.08 eV), respectively.	39
4.8	Structures from the diffusion process of a single nickel atom through a defective graphene sheet supported by three layers of Ir(111). Shown are the reactant state (a), the transition state (b) and the product state (c), respectively.	40
4.9	Angle-resolved photoemission spectra of (a) a Re surface, (b) Gr/Re and (c) Gr/Ag/Re, respectively. The measurements were conducted by M. Papagno and coworkers [45].	41
4.10	Energy [eV] vs. lattice constant [\AA], as employed numerically to determine the equilibrium lattice constant a of graphene. In these numerical runs, the optB88 functional was used to approximate the exchange-correlation functional.	43
4.11	Map of the energy [eV] vs. lattice constants a [\AA] and c/a , as employed to determine the equilibrium lattice constants a and c/a of Re. Darker colors correspond to a and c/a combinations which are lower in energy. In these runs, the optB88 functional was used as the exchange-correlation functional. \times indicates the minimum energy configuration.	44
4.12	Three different interface structures were considered in our numerical treatment of Gr/Ag/Re, namely top-hcp, top-fcc and hcp-fcc. a) and b) show the Gr/Ag/Re cell in a top and side view, respectively. The structural data stems from an actual simulation of graphene on a Ag/Re substrate employing the optB88 functional and was expanded from the 1x1 to a 4x4 cell to achieve better visibility.	46
4.13	Energy [eV] per Gr/Ag/Re unit cell versus graphene-substrate distance d [\AA], calculated by means of the optB88 functional for the two models employing the Re (left) and Gr (right) lattice constant and different interface geometries, respectively.	47

-
- 4.14 Bandstructure of Gr/Ag/Re, employing the equilibrium structures of the Re (left column) and the Gr model (right column) for the functional optB88. The radius of the circles corresponds to the degree of the state's localization. Included are graphene's π -bands (green) and the Ag d-bands (red), respectively. For the former, the radius of the circles has been multiplied by a factor of 5.5 to achieve better visibility, for the latter a factor of 2.5 was employed. The energy is shifted such that the Fermi energy E_F represents the reference energy. 49
- 4.15 Bandstructure of Gr/Ag/Re, employing the optB88 optimized top-fcc structure and equilibrium lattice constant of Re for a selection of different substrate-graphene distances d . The radius of the circles corresponds to the degree of the state's localization. Included are graphene's π -bands (green) and the Ag d-bands (red), respectively. For the former, the radius of the circles has been multiplied by a factor of 5.5 to achieve better visibility, for the latter a factor of 2.5 was employed. The energy is shifted such that the Fermi energy E_F represents the reference energy. 50
- 4.16 Bandstructure of Gr/Ag/Re from experiment [45] (a), of Gr/Ag/Re at a graphene-substrate distance of 3.4 Å (b), of Ag/Re (c) and Gr/Ag (d). The radius of the circles corresponds to the degree of the state's localization. Graphene's π -bands are colored green, silver's s - and d_{z^2} -bands blue and the remaining d -bands are colored red. The energy is shifted such that the Fermi energy E_F represents the reference energy. 51
- 4.17 Cell configuration of graphene supported by five (six) layers of rhenium, featuring a graphene-substrate distance of 5.4 Å (2.9 Å). The structure was expanded from the 1x1 to a 4x4 cell to achieve better visibility. . . 53
- 4.18 Bandstructure of graphene supported by five (six) layers of rhenium, featuring a graphene-substrate distance of 5.4 Å (2.9 Å). The radius of the circles corresponds to the degree of the state's localization. Graphene's π -bands are colored green. The different geometries correspond to the structures depicted in Fig. 4.17. The energy is shifted such that the Fermi energy E_F represents the reference energy. 53

List of Tables

4.1	Experimentally and numerically obtained equilibrium lattice constants a and energies per carbon atom of graphene, calculated for different exchange-correlation potential approximations.	43
4.2	Experimentally and numerically obtained lattice constants a and c/a and equilibrium energies per Re atom, calculated for different exchange-correlation potential approximations.	45
4.3	Comparison of the equilibrium lattice constants of rhenium and graphene, respectively.	45
4.4	Equilibrium graphene-substrate distances d in Å, tabulated for different functionals and interface structures. The left column corresponds to the toymodel emplying the lattice constant of rhenium ($a = a_{Re}$), the right column to the lattice parameter of graphene ($a = a_{Gr}$), respectively. .	48